



The Mitochondrial Ca²⁺ uniporter is a central regulator of interorganellar Ca²⁺ transfer and NFAT activation

Received for publication, May 12, 2021, and in revised form, August 31, 2021. Published, Papers in Press, September 6, 2021.
<https://doi.org/10.1016/j.jbc.2021.101174>

Ryan E. Yoast^{1,‡}, Scott M. Emrich^{1,‡}, Xuexin Zhang¹, Ping Xin^{1,2,3}, Vikas Arige⁴, Trayambak Pathak^{1,2,3}, J. Cory Benson^{1,2,3}, Martin T. Johnson¹, Ahmed Emam Abdelnaby^{1,2,3}, Natalia Lakomski¹, Nadine Hempel⁵, Jung Min Han⁶, Geneviève Dupont⁷, David I. Yule⁴, James Sneyd⁸, and Mohamed Trebak^{1,2,3,*}

From the ¹Department of Cellular and Molecular Physiology, The Pennsylvania State University College of Medicine, Hershey, Pennsylvania, USA; ²Department of Pharmacology and Chemical Biology and ³Vascular Medicine Institute, University of Pittsburgh School of Medicine, Pittsburgh, Pennsylvania, USA; ⁴Department of Pharmacology and Physiology, University of Rochester, Rochester, New York, USA; ⁵Department of Pharmacology, The Pennsylvania State University College of Medicine, Hershey, Pennsylvania, USA; ⁶Laboratory of Biological Modeling, National Institute of Diabetes and Digestive and Kidney Diseases, National Institutes of Health, Bethesda, Maryland, USA; ⁷Unité de Chronobiologie Théorique, Université Libre de Bruxelles, Brussels, Belgium; and ⁸Department of Mathematics, The University of Auckland, Auckland, New Zealand

Edited by Roger Colbran

Mitochondrial Ca²⁺ uptake tailors the strength of stimulation of plasma membrane phospholipase C-coupled receptors to that of cellular bioenergetics. However, how Ca²⁺ uptake by the mitochondrial Ca²⁺ uniporter (MCU) shapes receptor-evoked interorganellar Ca²⁺ signaling is unknown. Here, we used CRISPR/Cas9 gene knockout, subcellular Ca²⁺ imaging, and mathematical modeling to show that MCU is a universal regulator of intracellular Ca²⁺ signaling across mammalian cell types. MCU activity sustains cytosolic Ca²⁺ signaling by preventing Ca²⁺-dependent inactivation of store-operated Ca²⁺ release-activated Ca²⁺ channels and by inhibiting Ca²⁺ extrusion. Paradoxically, MCU knockout (MCU-KO) enhanced cytosolic Ca²⁺ responses to store depletion. Physiological agonist stimulation in MCU-KO cells led to enhanced frequency of cytosolic Ca²⁺ oscillations, endoplasmic reticulum Ca²⁺ refilling, nuclear translocation of nuclear factor for activated T cells transcription factors, and cell proliferation, without altering inositol-1,4,5-trisphosphate receptor activity. Our data show that MCU has dual counterbalancing functions at the cytosol-mitochondria interface, whereby the cell-specific MCU-dependent cytosolic Ca²⁺ clearance and buffering capacity of mitochondria reciprocally regulate interorganellar Ca²⁺ transfer and nuclear factor for activated T cells nuclear translocation during receptor-evoked signaling. These findings highlight the critical dual function of the MCU not only in the acute Ca²⁺ buffering by mitochondria but also in shaping endoplasmic reticulum and cytosolic Ca²⁺ signals that regulate cellular transcription and function.

In addition to their well-established role in cellular energy production and metabolism, mitochondria play a critical role in cellular signaling pathways that regulate gene transcription, cell survival, and function (1, 2). In particular, mitochondria

are active participants in cellular Ca²⁺ signaling (3–8). Mitochondrial Ca²⁺ uptake, which is driven by the steep voltage gradient across the inner mitochondrial membrane, occurs through a protein complex containing the pore-forming mitochondrial Ca²⁺ uniporter (MCU) protein (9, 10). MCU forms a Ca²⁺-selective tetrameric channel in the inner mitochondrial membrane that is regulated by the gate-keeping function of Ca²⁺-binding MICU1/2 protein dimers (11–16). MICU1/2 dimers keep the MCU channel closed under resting levels of free cytosolic Ca²⁺. Increased Ca²⁺ concentration in the vicinity of MCU and Ca²⁺ binding to the EF-hand domains of MICU1/2 disinhibits MCU channels and enhances mitochondrial Ca²⁺ uptake (13, 14). Ca²⁺ extrusion from the mitochondrial matrix to the cytosol occurs through independent transporters, which include the mitochondrial Na⁺/Ca²⁺ exchanger (NCLX) (17) and possibly the Ca²⁺/H⁺ exchanger Letm1 (18). The gatekeeping of MCU channel activity by MICU1/2 is relieved only when cytosolic Ca²⁺ concentration is high (above ~1.3 μM and above 500 nM when only MICU1 is present (13), but see also (14) where calculated K_d for Ca²⁺ binding to MICU1/2 dimers is ~650 nM). As such, mitochondrial Ca²⁺ uptake is thought to take place at specialized microdomains where cytosolic Ca²⁺ concentrations are high. Such microdomains include the mitochondria-associated membranes (MAMs) where the endoplasmic reticulum (ER) membrane is within 10 to 30 nm from the outer mitochondrial membrane and Ca²⁺ is transferred to mitochondria through closely apposed inositol-1,4,5-trisphosphate receptor (IP₃R) channels within ER membranes (19).

Activation of plasma membrane (PM) receptors that couple to isoforms of phospholipase C by hormones, neurotransmitters, and growth factors causes the breakdown of membrane-associated phosphatidylinositol-4,5-bisphosphate into two second messengers: the membrane-bound diacylglycerol and the diffusible IP₃ (20). Activation of IP₃R channels located in the ER causes ER Ca²⁺ store depletion. Upon Ca²⁺ store depletion, ER-resident stromal interaction molecules 1 and 2

[‡] These authors contributed equally to this work.

* For correspondence: Mohamed Trebak, trebakm@pitt.edu.

(STIM1/2) undergo a conformational change and move to ER-PM junctional spaces where they form puncta and activate Orai channels mediating the highly Ca²⁺-selective, store-operated, Ca²⁺ release-activated Ca²⁺ (CRAC) current (21–23). Under conditions of stimulation with low concentrations of receptor agonists believed to represent physiological levels of receptor stimulation, cytosolic Ca²⁺ signals manifest as regenerative Ca²⁺ oscillations, which result from cycles of Ca²⁺ release through IP₃R and concomitant bursts of CRAC channel activities that, depending on the cell type, can either directly sustain Ca²⁺ oscillations or replenish the depleted ER stores to sustain IP₃R-driven Ca²⁺ oscillations (24–26). Local Ca²⁺ entry through Orai/CRAC channels leads to the activation of isoforms of the nuclear factor for activated T cells (NFAT) transcription factors (27), which activate gene programs that control various cell functions, including proliferation and metabolism (28, 29).

As Ca²⁺ enters through CRAC channels and accumulates on the cytosolic side of the PM, it mediates inhibition of CRAC channels through several feedback mechanisms. First, there is fast Ca²⁺-dependent inactivation (CDI) that involves Ca²⁺ binding to inhibitory sites within few nanometers of the mouth of CRAC channels (30–33). Mitochondria locate within 100 to 500 nm from the PM, and because of their size, they would be presumably excluded from the tight ER-PM junctional sites that span ~10 to 25 nm where STIM and Orai coaggregate. Therefore, it is unlikely that mitochondria can affect fast CDI of CRAC channels in any meaningful way. Second, there is slow CDI that is triggered by store refilling (34), which is due to reversal of STIM puncta independently of mitochondria. Third, there is another form of slow CDI that occurs independently of store refilling (*e.g.*, in the presence of thapsigargin) (34). This store-independent slow CDI is mediated by Ca²⁺-binding sites that are located ~100 nm or more from CRAC channels (34) and was proposed to be mediated by Ca²⁺-calmodulin (CaM)-mediated dissociation of STIM1 puncta and STIM1–Orai1 complexes (35). This latter form of slow CDI could be presumably prevented by mitochondrial Ca²⁺ buffering at a distant microdomain where CaM is located. Indeed, previous studies pre-dating the discovery of MCU and STIM–Orai have used drugs such as carbonyl cyanide *m*-chlorophenylhydrazone (CCCP) and antimycin A1, which inhibit mitochondrial Ca²⁺ uptake by altering mitochondrial respiration or depolarizing its membrane, to propose that mitochondria can buffer Ca²⁺ to alleviate slow CDI and sustain store-operated Ca²⁺ entry (SOCE) in Jurkat and primary T cells (36, 37). A more recent study utilized MCU knockdown with siRNA in rat basophilic leukemia (RBL) cells and suggested that mitochondrial Ca²⁺ buffering specifically by MCU is required for sustaining the activity of IP₃R, CRAC channels, and agonist-evoked Ca²⁺ oscillations (38).

Here, we have investigated the role of MCU in regulating cytosolic, ER, and mitochondrial Ca²⁺ dynamics using an arsenal of cell lines and primary cells from different species and tissues. We utilized CRISPR/Cas9 to produce several clones of MCU knockout in cultured cells and used the Cre-LoxP system to generate populations of primary cells from

tissue-specific MCU knockdown mice. We show that, despite promoting slow CDI of CRAC channels and enhancing cytosolic Ca²⁺ extrusion, MCU deletion leads to enhanced cytosolic Ca²⁺ in response to passive store depletion. MCU-KO also enhanced the frequency of cytosolic Ca²⁺ oscillations in response to agonist stimulation without affecting IP₃R-mediated Ca²⁺ puffs. MCU-KO causes enhanced ER Ca²⁺ refilling and increased nuclear translocation of NFAT isoforms and increased B-lymphocyte proliferation. Mathematical modeling is consistent with MCU as an important regulator of interorganellar Ca²⁺ transfer that fine-tunes cytosolic Ca²⁺ signaling. Our data provide critical insights into the role of MCU and mitochondrial Ca²⁺ uptake in cellular signaling. Despite the critical function of MCU-mediated mitochondrial Ca²⁺ uptake in inhibiting CRAC channel slow CDI and limiting Ca²⁺ extrusion, MCU deletion leads to a paradoxical enhancement of cytosolic Ca²⁺ upon receptor stimulation. Thus, the inability of mitochondria to store its “allocated share” of Ca²⁺ in the absence of MCU offsets the effects on Ca²⁺ extrusion and CRAC channel activity. The net result of MCU-KO is enhanced ER Ca²⁺ refilling and increased cytosolic Ca²⁺ signaling. Our data show that MCU has dual counterbalancing functions at the cytosol–mitochondria interface. MCU activity can enhance near PM Ca²⁺ signaling to increase NFAT activity and can also inhibit NFAT activity through the “Ca²⁺ sink” effect of mitochondria. This reciprocal regulation by MCU fine-tunes interorganellar Ca²⁺ transfer and NFAT activation during receptor-evoked signaling.

Results

MCU knockout enhances cytosolic Ca²⁺ despite promoting Ca²⁺ extrusion and CRAC channel slow CDI

We performed CRISPR/Cas9 gene knockout of MCU in six cell lines from different tissues and species (Fig. 1). A seventh cell line (HeLa) and its corresponding MCU CRISPR/Cas9 knockout clone were kindly provided by Dr Suresh Joseph (Thomas Jefferson University) (Fig. S1). The cell lines are human HeLa, embryonic kidney (HEK293), colorectal cancer HCT116 and DLD1, and Jurkat T cells, rat basophilic leukemia (RBL-1) mast cells, and mouse A20 B cells. These MCU knockout cell lines provided a clean background to analyze the role of mitochondrial Ca²⁺ uptake in shaping intracellular Ca²⁺ signaling. To alleviate potential off-target effects of CRISPR/Cas9 KO, we studied two independent MCU-KO clones for each cell line (except for HeLa cells, of which we obtained only one clone). These clones were identified; validated for MCU-KO with genomic sequencing, Western blot, and mitochondrial Ca²⁺ measurements; and assayed in parallel to their corresponding parental controls. Absence of the MCU protein in knockout cells was documented by Western blot (Fig. 1, A, C, E, G, I, and K). Functional knockout of MCU was documented by simultaneous Ca²⁺ and mitochondrial membrane potential fluorescence measurements in a permeabilized cell system (Fig. S2). The addition of a bolus 10 μM Ca²⁺ to the bath of permeabilized parental cells resulted in rapid mitochondrial uptake, which did not occur in MCU-KO cells,

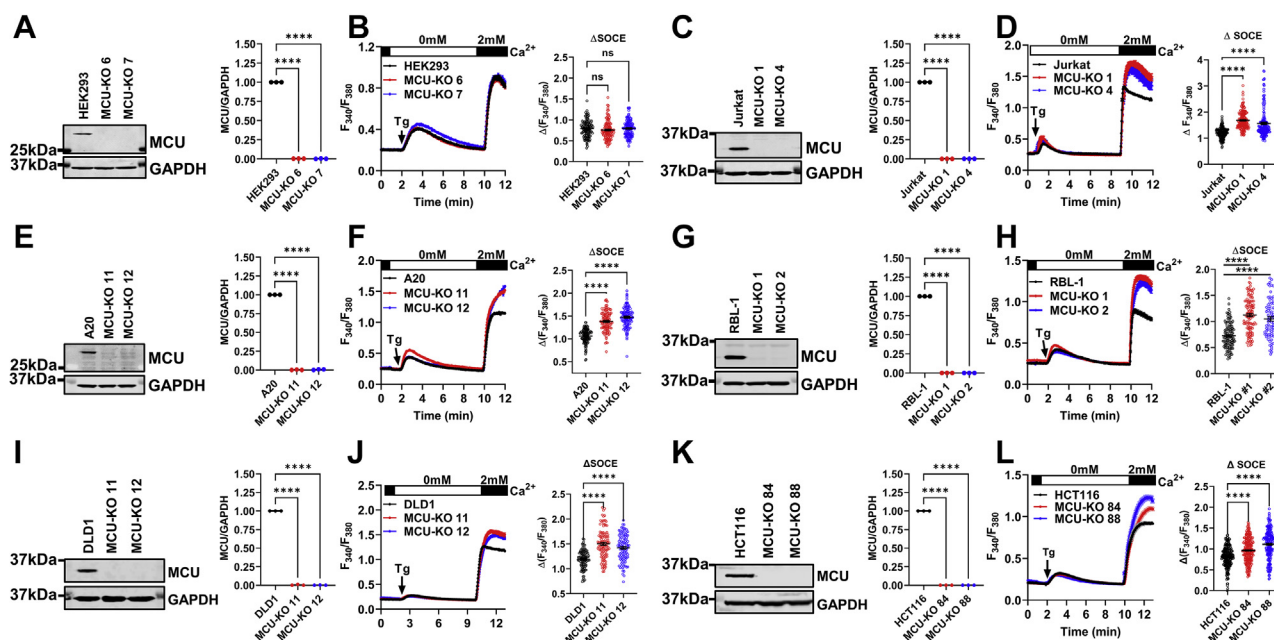


Figure 1. MCU-KO enhances cytosolic Ca²⁺ upon thapsigargin stimulation. Western blot documenting MCU protein knockout in two independent CRISPR/Cas9 MCU-KO clones of HEK293 cells and quantification of MCU protein band densitometry relative to GAPDH from three independent experiments (A). Ca²⁺ measurements in HEK293 parental cells and MCU-KO clones in response to stimulation with 2 μM thapsigargin (Tg) in Ca²⁺-free buffer followed by restoration of 2 mM extracellular Ca²⁺ to determine the magnitude of SOCE (B). Quantification of SOCE (Δ SOCE) from at least three independent experiments are also shown (B) (n = 120; each point represents one cell). Identical experiments to (A and B) were performed in human Jurkat T cells (C and D) (n = 167–178), mouse A20 B cells (E and F) (n = 114–119), rat RBL-1 mast cells (G and H) (n = 82–115), human DLD1 colorectal carcinoma cells (I and J) (n = 104–112), and human HCT116 colorectal carcinoma cells (K and L) (n = 203–229). All Western blot data (A, C, E, G, I, and K) are representative of three independent runs (n = 3). Statistical significance was determined using an ordinary one-way ANOVA where ****p < 0.0001. SOCE data are represented as the mean ± SEM and were statistically analyzed using a Kruskal–Wallis one-way ANOVA with multiple comparisons with their corresponding parental cell line where ****p < 0.0001; ns, not significant p > 0.05. MCU, mitochondrial Ca²⁺ uniporter; SOCE, store-operated Ca²⁺ entry.

demonstrating that acute mitochondrial Ca²⁺ uptake was abrogated in MCU-KO cells (Fig. S2).

The predominant receptor-activated Ca²⁺ entry pathway in all seven nonexcitable cell lines considered herein is the SOCE pathway, which biophysically manifests as the CRAC current encoded by STIM1/2 and Orai1/2/3 proteins. To maximally activate SOCE, we irreversibly blocked the sarcoplasmic/ER Ca²⁺ ATPase (SERCA) using thapsigargin (Tg; 2 μM), which causes passive depletion of ER Ca²⁺ stores (recorded in Ca²⁺-free bath solutions) and activation of SOCE, which manifests upon addition of 2 mM Ca²⁺ to the extracellular bath (Fig. 1, B, D, F, H, J, and L). Surprising, the use of this protocol revealed that MCU-KO led to a significant increase in apparent SOCE in all cell lines, with the exception of MCU-KO HEK293 cells where SOCE was increased in some runs but not significantly different from that of the parental HEK293 cells when all cells were averaged (Fig. 1B; see also Fig. 2A). This notable difference between HEK293 cells and the other six cell lines will be addressed further below. Western blots showed no change in STIM1 protein levels upon MCU-KO in either HEK293 cells or Jurkat cells (Fig. S3). Quantitative PCR analysis revealed no significant compensatory up/downregulation of all five STIM–Orai proteins in HEK293 or Jurkat MCU-KO cells (Fig. S4).

Previous reports showed that abrogation of the ability of mitochondria to buffer cytosolic Ca²⁺, through dissipation of the mitochondrial membrane potential by the protonophore carbonyl cyanide m-chlorophenylhydrazone (CCCP) or

blockade of complex III and complex V of the electron transport chain with Antimycin A1 and oligomycin, led to inhibition of SOCE (37). CRAC currents were also inhibited by these drugs, when recorded with either the perforated patch-clamp technique or the whole-cell technique with pipette solutions containing a relatively low Ca²⁺ buffer (1.2 mM EGTA) but including metabolites that promote energized mitochondria (36). These findings showed that a healthy mitochondrial membrane potential supports mitochondrial Ca²⁺ uptake, which in turn limits slow Ca²⁺-dependent inhibition (CDI) of CRAC channels to sustain SOCE.

Therefore, we performed SOCE measurements in response to thapsigargin in parental HEK293, Jurkat, and RBL-1 cells and their MCU-KO counterparts and tested the effect of 5 μM of the protonophore trifluoromethoxy carbonylcyanide phenylhydrazone (FCCP) on SOCE. As seen in Figure 2, A–C, when added after SOCE was initiated, FCCP significantly inhibited SOCE in both parental cells and their MCU-KO counterparts. The inhibition of SOCE in parental Jurkat (Fig. 2B) and RBL-1 (Fig. 2C) cells was slower than in their MCU-KO counterparts and was preceded by a transient increase in Ca²⁺, presumably reflecting bigger mitochondrial Ca²⁺ stores in the parental cells. In HEK293 cells, the rate of SOCE inhibition by FCCP was similar between wildtype and MCU-KO cells (Fig. 2A), suggesting a bigger contribution of mitochondria as a reservoir for Ca²⁺ in Jurkat and RBL-1 cells compared with HEK293 cells. Addition of 1 μM ionomycin to HEK293 and Jurkat cells (red arrow; Fig. 2, A and B) to release

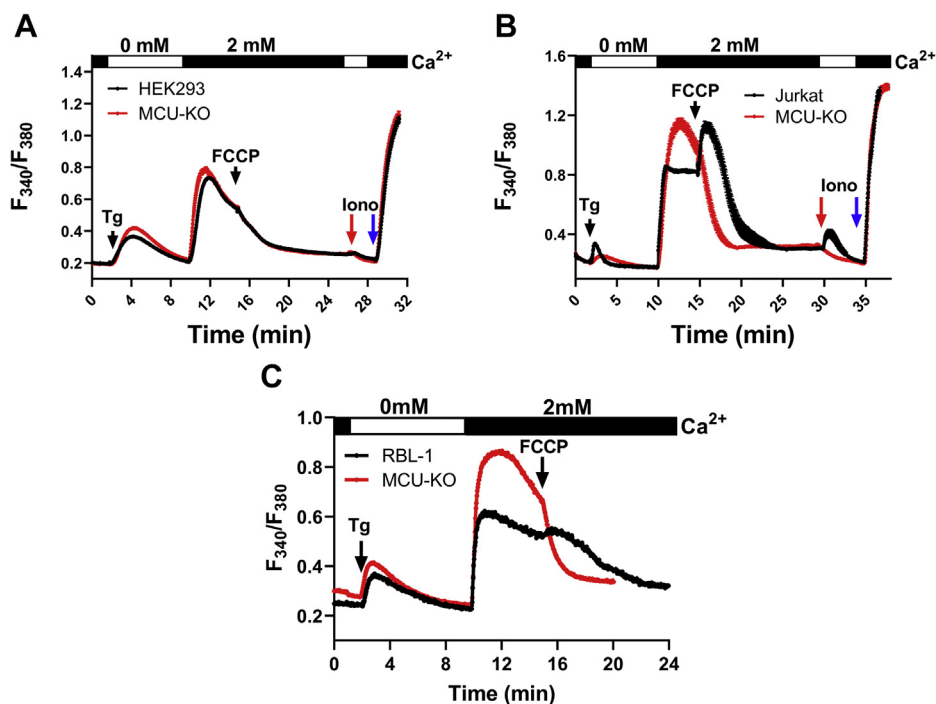


Figure 2. Dissipation mitochondrial membrane potential inhibits store-operated Ca^{2+} entry in wildtype and MCU-KO cells. A–C, Fura2 Ca^{2+} measurements using 2 μM thapsigargin first in the absence then presence of 2 mM extracellular Ca^{2+} in wildtype and MCU-KO HEK293 (A), Jurkat (B), and RBL-1 (C) cells. Addition of 5 μM FCCP to cells after Ca^{2+} entry is initiated, followed in (A and B) by 1 μM ionomycin in 0 mM external Ca^{2+} (red arrow), then 10 μM ionomycin in 2 mM external Ca^{2+} solution (blue arrow). Cytosolic Ca^{2+} traces in (A–C) represent \pm SEM of $n = 43$ to 156 individual cells. MCU, mitochondrial Ca^{2+} uniporter.

any remaining Ca^{2+} from thapsigargin-independent stores (presumably mitochondria) showed a small mitochondrial Ca^{2+} release in wildtype Jurkat cells but not in wildtype HEK293 cells. We subsequently added 10 μM ionomycin (blue arrow) in the presence of 2 mM Ca^{2+} to confirm that maximal Fura2 signal is equal between MCU-KO and parental cells. Overall, these data argue that inhibition of SOCE by FCCP cannot be explained simply by lack of mitochondrial Ca^{2+} buffering through MCU. One recurring observation in our recordings is the enhanced rate of decline of SOCE steady-state plateaus in Jurkat and RBL-1 MCU-KO cells compared with parental cells (Fig. 2, B and C), suggesting that mitochondrial Ca^{2+} buffering by MCU inhibits PM Ca^{2+} ATPase-mediated Ca^{2+} extrusion, as shown previously in Jurkat T cells (39). Indeed, inhibition of SOCE with 5 μM Gd^{3+} revealed that the rate of Ca^{2+} extrusion is significantly faster in MCU-KO cells compared with Jurkat (Fig. 3, A and B) and RBL-1 parental cells (Fig. 3, C and D).

We then sought to determine whether increased SOCE upon MCU-KO is due to increased net CRAC currents across the PM by using the whole-cell patch clamp technique. We chose to record from two widely studied cell lines that produce the largest native CRAC currents, namely, Jurkat and RBL-1 cells. We recorded both Ca^{2+} CRAC currents in 20 mM Ca^{2+} bath solutions and performed rapid switches to divalent-free bath solutions to record Na^{+} CRAC currents, which are larger in size. We measured whole-cell CRAC currents from Jurkat and RBL-1 cells under two different conditions. The first condition uses a pipette solution with a

low buffering capacity (1 mM EGTA) that includes 30 μM IP₃ to empty the stores and contains a cocktail of mitochondria-energizing metabolites (see Methods) that can reveal potential mitochondrial effects on CRAC channel slow CDI. The second condition uses a pipette solution with a very strong buffer (50 mM BAPTA) that would negate any potential effect of mitochondrial Ca^{2+} buffering on CRAC currents. Native Ca^{2+} and Na^{+} CRAC currents under both weak and strong buffer conditions in MCU-KO clones of both Jurkat and RBL-1 cells were statistically of similar magnitude compared with currents from their corresponding parental cells (Fig. 4). To accurately determine if MCU deletion alters store-independent CRAC channel slow CDI, we used an established patch clamp protocol where Jurkat cells were preincubated with thapsigargin in the absence of extracellular Ca^{2+} and I_{CRAC} was recorded on introduction of 20 mM Ca^{2+} to the bath solution (34). I_{CRAC} was recorded in both Jurkat MCU-KO and parental cells with a pipette solution containing a low buffer (1.2 mM EGTA, 0.66 mM Ca^{2+} (34); see Experimental procedures) either with or without supplementation with the mitochondria-energizing cocktail (Fig. 5). Of interest, even in the absence of the mitochondria-energizing cocktail, MCU-KO cells showed enhanced slow CDI compared with control cells (Fig. 5, A–C). Furthermore, when the pipette solution included the mitochondria-energizing cocktail, I_{CRAC} slow CDI of parental Jurkat cells was inhibited on average by $\sim 90\%$, whereas I_{CRAC} slow CDI in MCU-KO cells remained unchanged (Fig. 5, D–F). CDI recordings with and without mitochondria-energizing cocktail

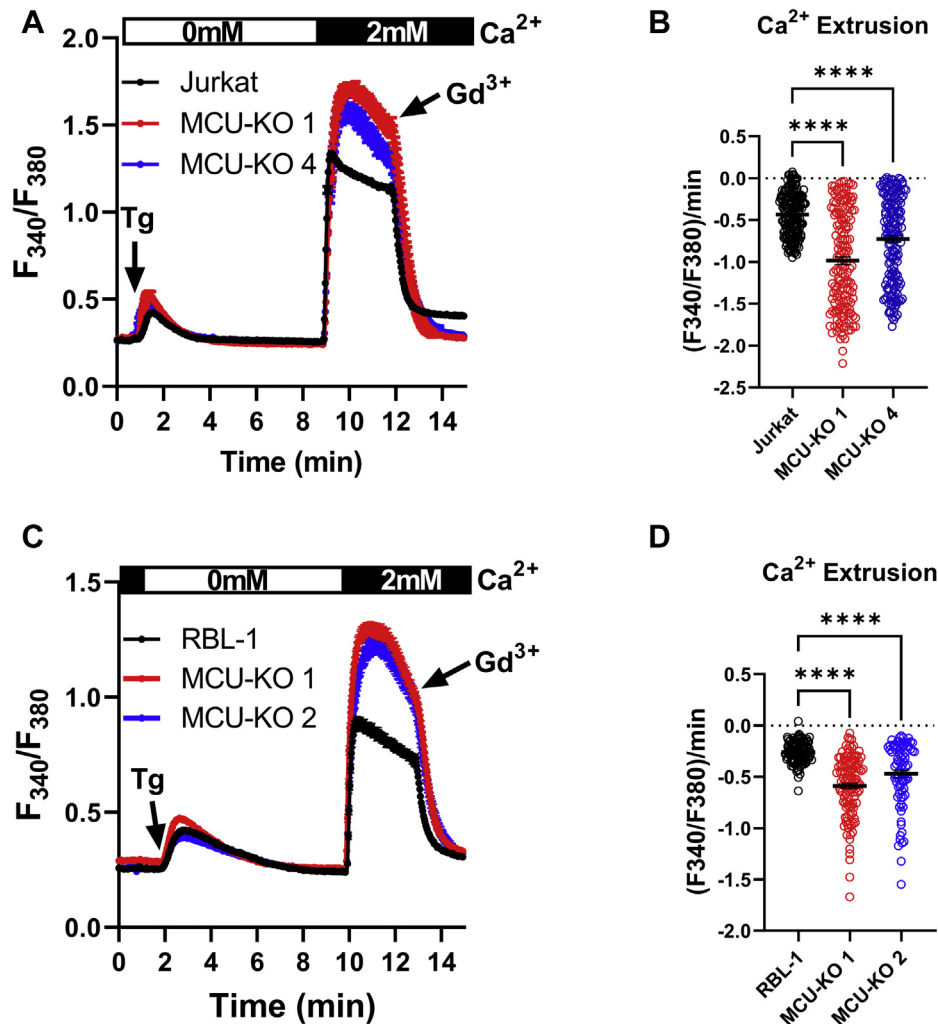


Figure 3. MCU-KO enhances Ca^{2+} extrusion. MCU-KO and parental Jurkat (A and B) and RBL-1 (C and D) cells were stimulated with 2 μM Tg in Ca^{2+} -free buffer followed by restoration of 2 mM extracellular Ca^{2+} to determine the magnitude of store-operated Ca^{2+} entry followed by addition of 5 μM Gd^{3+} to block store-operated Ca^{2+} entry and assess Ca^{2+} extrusion. The slope of Ca^{2+} extrusion in these cells was calculated and reported statistically in (B and D). Statistical significance was determined using the Kruskal-Wallis one-way ANOVA with multiple comparisons to their corresponding parental cell line where **** p < 0.0001. Cytosolic Ca^{2+} traces in (A and C) represent \pm SEM of $n = 82$ to 178 individual cells. MCU, mitochondrial Ca^{2+} uniporter.

in each individual wildtype Jurkat and MCU-KO cell are shown in Figures S5 and S6, respectively.

Taken together, these data indicate that, although abrogation of MCU-mediated mitochondrial Ca^{2+} uptake promotes Ca^{2+} extrusion and CRAC channel CDI, its net effect is an increase, rather than a decrease, in cytosolic Ca^{2+} levels. Our findings suggest that preventing mitochondria from buffering its allocated share of cytosolic Ca^{2+} could lead to accelerated ER Ca^{2+} refilling and enhanced frequency of agonist-evoked cytosolic Ca^{2+} oscillations, NFAT activation, and cell proliferation. These concepts are explored further below.

MCU knockout enhances the frequency of cytosolic Ca^{2+} oscillations without affecting IP_3R activity

We determined the effect of MCU-KO on Ca^{2+} signaling triggered by physiological agonist stimulation. To induce cytosolic Ca^{2+} oscillations, Jurkat cells were stimulated with a relatively low concentration (0.125 $\mu\text{g}/\text{ml}$) of anti-CD3

antibody, which is commonly used to activate the T cell receptor and drive clonal expansion and interleukin 2 (IL-2) production. Under these conditions, essentially all Jurkat cells that responded displayed regenerative Ca^{2+} oscillations (Fig. 6, A and B) with MCU-KO Jurkat cells displaying enhanced frequency of Ca^{2+} oscillations compared with the parental cells (Fig. 6, A–C). Furthermore, Ca^{2+} oscillations in MCU-KO Jurkat cells were of longer duration compared with those of the parental cells (Fig. 6, D and E).

Stimulation of HEK293 with a low concentration of carbachol (CCh) (10 μM CCh), in the presence of 2 mM extracellular Ca^{2+} , evoked regenerative Ca^{2+} oscillations in the majority of cells (Fig. 6, F and I–K). Note that HEK293 cells were the only cell line studied where SOCE in response to thapsigargin was not significantly enhanced by MCU-KO. Yet, MCU-KO HEK293 cells showed a higher proportion of cells responding with a Ca^{2+} plateau at the expense of cells responding with repetitive Ca^{2+} oscillations compared with their parental counterparts (Fig. 6, I–K). Furthermore, when

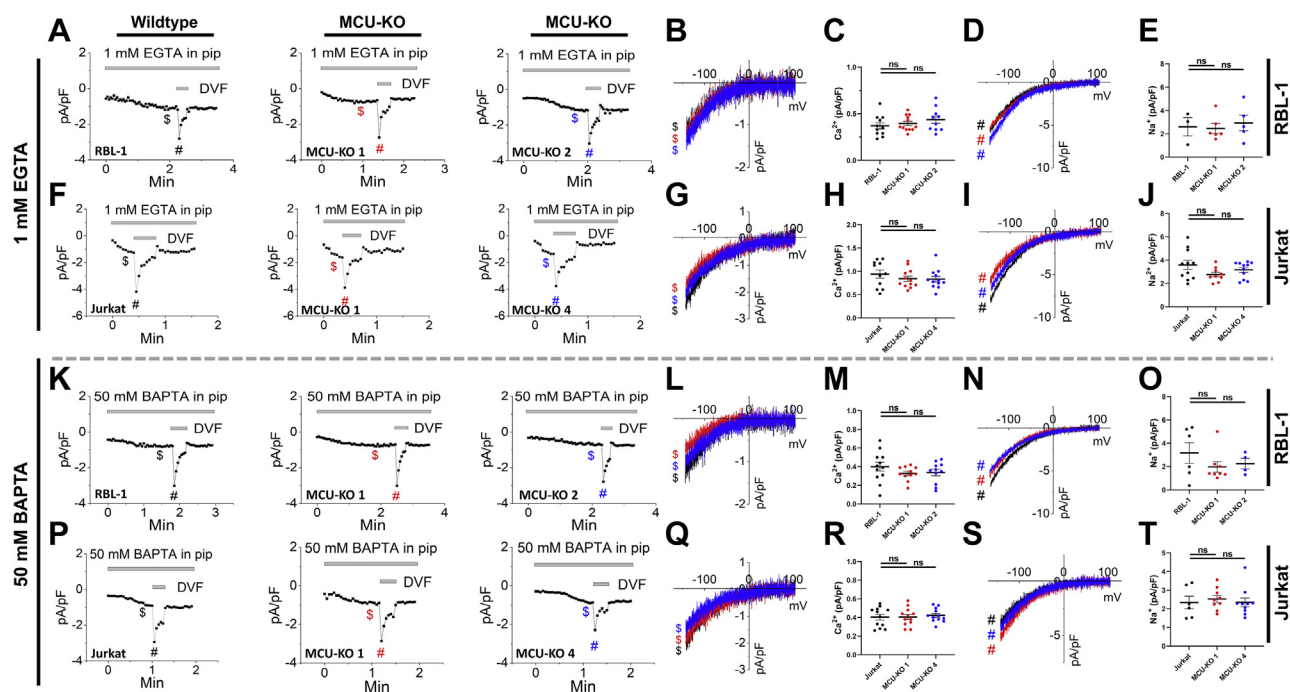


Figure 4. Effect of MCU-KO on CRAC currents. A, CRAC current development taken at -100 mV in (from left to right) parental RBL-1 mast cells, MCU-KO clone #1, and MCU-KO clone #2 of the same cells. Recordings were initiated after break-in with a pipette solution containing 1 mM EGTA and a mitochondria-energizing cocktail (see [Experimental procedures](#)). B and C, I-V relationship taken from traces in (A) were indicated by color-coded S signs (B), and quantification of peak CRAC current density (C) ($n = 10-12$) was recorded in 20 mM Ca^{2+} -containing bath solutions. D and E, ($n = 3-5$), similar data to (B and C) but for Na^+ CRAC currents recorded in divalent-free (DVF) solutions and I-V curves taken were indicated by the # signs. F-J, similar recordings and data analysis to (A-E) for parental Jurkat T cells and their MCU-KO clone #1 and clone #4. K-T, ($n = 6-12$), similar recordings and data analysis in parental and MCU-KO RBL-1 and Jurkat cells to (A-J) but using a pipette solution containing 50 mM BAPTA. All CRAC current data were analyzed using a Kruskal-Wallis one-way ANOVA with multiple comparisons to the corresponding parental cell line where ns, not significant $p > 0.05$. CRAC, Ca^{2+} release-activated Ca^{2+} ; MCU, mitochondrial Ca^{2+} uniporter.

oscillating cells are considered MCU-KO HEK293 cells showed a higher frequency of cytosolic Ca^{2+} oscillations than their parental counterparts (Fig. 6H), suggesting that MCU-KO leads to higher cytosolic Ca^{2+} . It is not obvious why the

cytosolic Ca^{2+} signal in response to thapsigargin is similar between MCU-KO HEK293 cells and their parental counterparts (despite clear differences in Ca^{2+} oscillations triggered by agonist). We reasoned that differences in mitochondrial and/

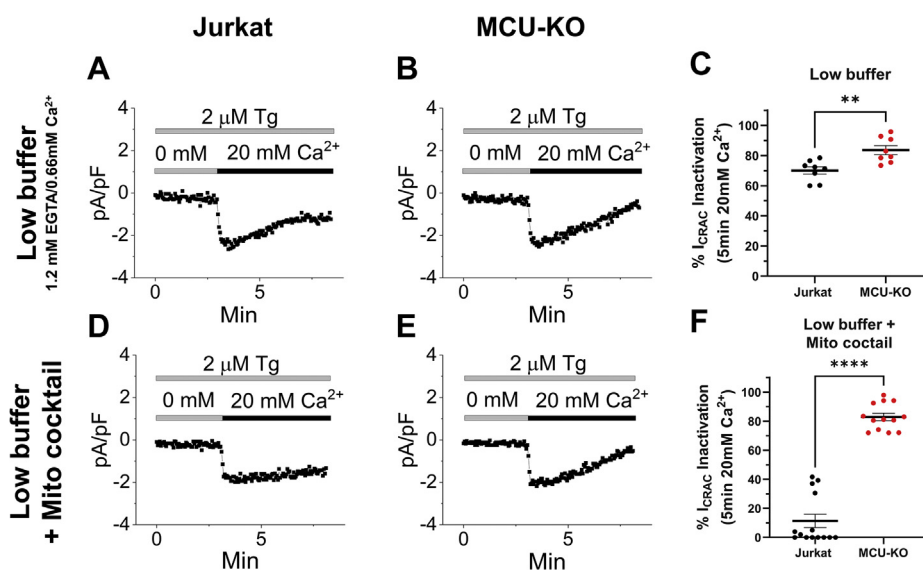


Figure 5. MCU-KO promotes slow CDI of CRAC currents. Slow CDI of CRAC currents recorded in parental Jurkat cells (A and D) and their MCU-KO counterparts (B and E) with a pipette solution containing 1.2 mM EGTA and 0.66 mM Ca^{2+} in either the presence (D and E) or absence (A and B) of the mitochondria-energizing cocktail. Percentage of CDI is reported for all conditions in (F, $n = 8$; F, $n = 13-14$). All CRAC current data are representative of at least three independent experiments and were analyzed using a Mann-Whitney test where $**p < 0.01$ and $****p < 0.0001$. CDI, Ca^{2+} -dependent inactivation; CRAC, Ca^{2+} release-activated Ca^{2+} ; MCU, mitochondrial Ca^{2+} uniporter.

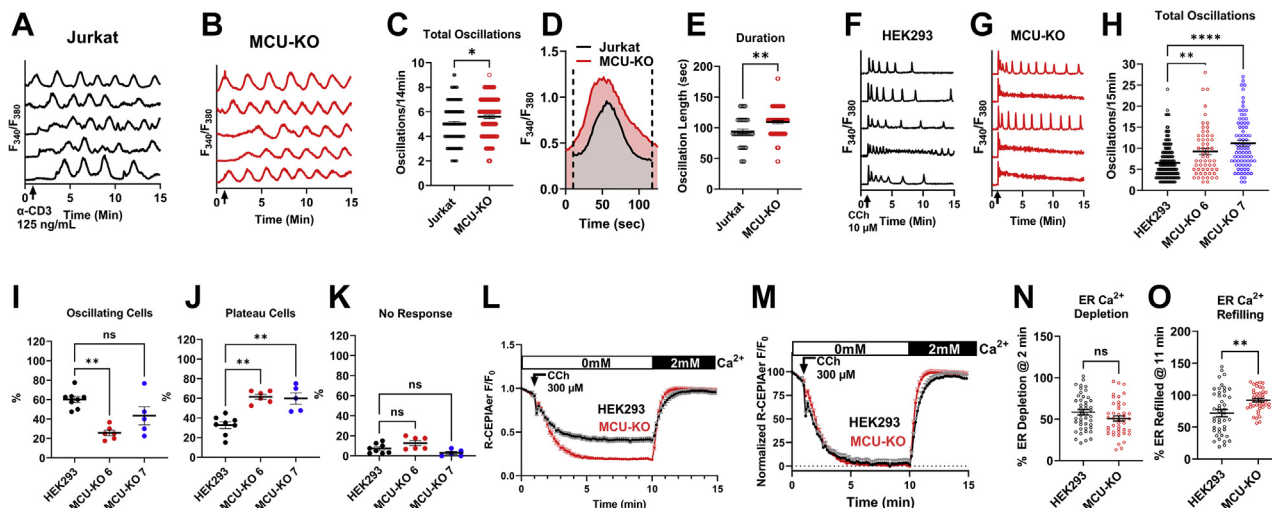


Figure 6. MCU-KO enhances the frequency of Ca^{2+} oscillations and ER refilling. A–E, Ca^{2+} oscillations were elicited in wildtype Jurkat cells (A) and their MCU-KO counterparts (B) by stimulation with 0.125 μ g/ml of anti-CD3 antibody in Ca^{2+} -containing (2 mM) buffer. The number of Ca^{2+} oscillations/14 min (C; $n = 114$ –122), overlaid representative spikes (D), and quantification of oscillation duration in seconds (E; $n = 40$ –81) in Jurkat cells and their MCU-KO variant are represented. Both oscillation frequency and duration data were analyzed using a Mann–Whitney test where $*p < 0.05$ and $*p < 0.01$. F–K, Ca^{2+} oscillations were elicited in wildtype HEK293 cells (F) and their MCU-KO counterparts (G) by stimulation with 10 μ M carbachol (CCh) in Ca^{2+} -containing (2 mM) buffer. H, ($n = 58$ –186) quantification of the number of oscillations/14 min in wildtype HEK293 cells and their MCU-KO clones #6 and #7. Quantification of the percentage of HEK293 cells and MCU-KO cells that respond with either repetitive Ca^{2+} oscillations (I; $n = 5$ –8) or sustained Ca^{2+} plateaus (J; $n = 5$ –8) as well as cells that show no response (K; $n = 5$ –8). All HEK293 oscillation data were analyzed for statistical significance using the Kruskal–Wallis test where $**p < 0.01$; and ns, not significant $p > 0.05$. L–N, direct measurements of ER Ca^{2+} levels using CEPIAer in HEK293 cells and their MCU-KO counterparts. Cells were stimulated with 300 μ M CCh in Ca^{2+} -free buffer to elicit ER Ca^{2+} depletion followed by CCh washout and replenishment of 2 mM Ca^{2+} to measure ER refilling (L). Data in (L) are normalized in (M) and rates of ER depletion (N) and refilling (O). Rates of ER depletion are represented as \pm SEM of $n = 43$ to 45 individual cells; resulting data from these traces were analyzed using an unpaired t test where $*p < 0.05$, $****p < 0.0001$, and ns, not significant $p > 0.05$. All data are representative of at least three independent experiments. ER, endoplasmic reticulum; MCU, mitochondrial Ca^{2+} uniporter.

or cytosolic volumes between these different cells might play a role. We performed high-resolution three-dimensional multi-spectral confocal microscopy to generate volumetric reconstructions of the cytosol and mitochondria of Jurkat, A20, RBL-1, and HEK293 cell lines (Fig. 7, A–E). Our volumetric measurements showed that HEK293 cells have a higher surface

area and cytosolic and cell volume compared with all other cell lines (Fig. 7, A–G). However, we found no obvious correlation between the mitochondrial volume or the mitochondria/cell ratio and the differences in SOCE in response to thapsigargin between parental and MCU-KO cells (Fig. 7, D and E). Of interest, side-by-side comparisons of mitochondrial Ca^{2+}

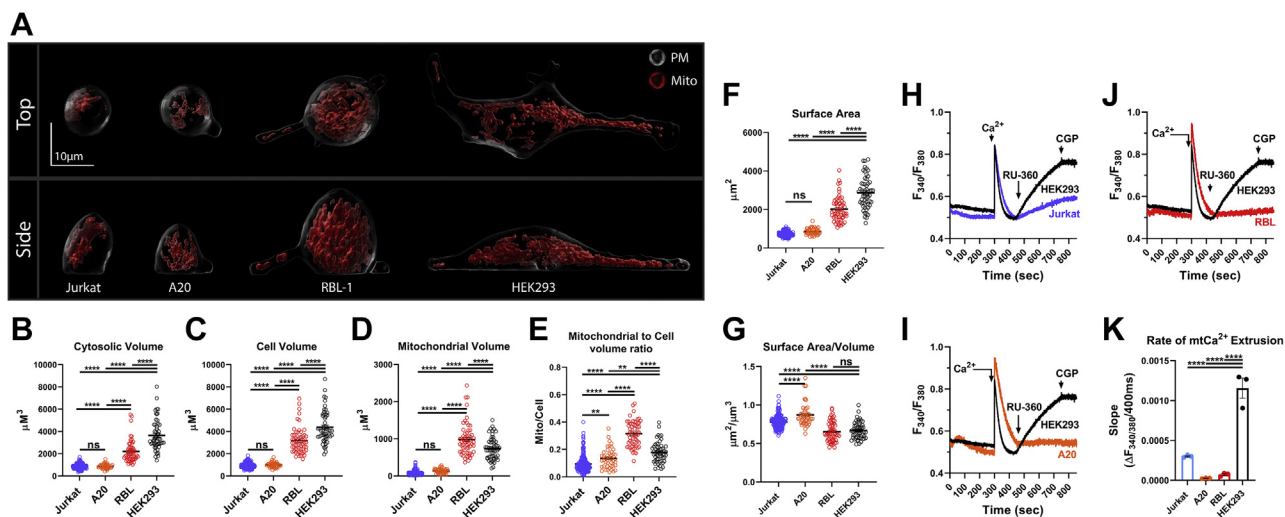


Figure 7. Cell and mitochondrial volume and Ca^{2+} extrusion differ between different cell lines. A, representative three-dimensional rendering of mitochondrial volume (red) relative to total cell volume in wildtype Jurkat, A20, RBL-1, and HEK293 cells. Cytosolic (B), cell (C), and mitochondrial (D) volumes, mitochondrial/cell volume ratio (E), surface area (F), and surface area/volume ratios (G) were calculated and statistically analyzed using a one-way ANOVA where $**p < 0.01$, $****p < 0.0001$, and ns, not significant $p > 0.05$. For all volume measurements $n = 44$ to 209. Mitochondrial Ca^{2+} extrusion was quantified for HEK293 comparing Jurkat (H), A20 (I), and RBL-1 (J) cells using a permeabilized cell system. Bolus 10 μ M Ca^{2+} was added to allow Ca^{2+} uptake, followed by addition of the MCU inhibitor RU360 (1 μ M) to determine the rate of mitochondrial Ca^{2+} extrusion. The NCLX inhibitor, CGP37157 (10 μ M), was added at the end of the recordings. (K; $n = 3$), Mitochondrial Ca^{2+} extrusion was calculated and statistically analyzed using a one-way ANOVA where $****p < 0.0001$. All data are representative of at least three independent experiments.

extrusion between wildtype HEK293, Jurkat, A20, and RBL-1 cells using the permeabilized cell preparation showed that HEK293 cells have significantly enhanced mitochondrial Ca^{2+} extrusion compared with all other cell types (Fig. 7, H–K). The enhanced mitochondrial Ca^{2+} extrusion in HEK293 cells suggests a moderate role of mitochondria in buffering cytosolic Ca^{2+} in these cells (see also Fig. 2A where FCCP effect is similar between parental and MCU-KO HEK293 cells). This might contribute to the blunting of small differences in the Ca^{2+} signal between MCU-KO and parental HEK293 cells under the thapsigargin protocol. Additional studies are needed to resolve this issue.

We also performed measurements of ER Ca^{2+} stores in MCU-KO and wildtype HEK293 cells by transiently expressing the genetically encoded Ca^{2+} sensor R-CEPIAer. Treatment of cells with supramaximal concentration of carbachol (300 μM CCh) in Ca^{2+} -free solution caused a significantly bigger drop of CEPIAer fluorescence in MCU-KO cells compared with parental cells (Fig. 6L), suggesting a higher ER Ca^{2+} content in MCU-KO cells compared with parental cells. These CEPIAer fluorescence measurements are represented as normalized data in Figure 6M. We did not resolve a difference in the rate of ER Ca^{2+} depletion between wildtype and MCU-KO HEK293 cells (Fig. 6N). However, the rate of ER Ca^{2+} refilling after CCh wash-off and addition of 2 mM Ca^{2+} to the bath was significantly faster in MCU-KO HEK293 cells (Fig. 6O), suggesting that MCU function limits cytosolic Ca^{2+} and ER Ca^{2+} content.

To determine whether enhanced Ca^{2+} oscillatory frequency of MCU-KO cells is due to increased IP_3R activity, we used total internal reflection fluorescence (TIRF) microscopy to

measure the elementary Ca^{2+} signals called Ca^{2+} puffs, which are mediated by IP_3Rs . We loaded parental HEK293 and MCU-KO cells with a Ca^{2+} dye and caged IP_3 (ci- IP_3/PM ; see Experimental procedures), and Ca^{2+} puffs were recorded at a rate of 166 frames/s upon photolysis of ci- IP_3 . We detected Ca^{2+} puffs in both parental HEK293 and MCU-KO cells following photolysis of ci- IP_3 (Fig. 8). However, the number of puffs and the number of puff sites recorded in either Ca^{2+} -free or Ca^{2+} -containing bath solutions were not significantly different between MCU-KO cells and parental HEK293 cells (Fig. 8, A, B, F, and G). The amplitude distribution of puffs did not differ between HEK293 and MCU-KO cells with most puffs ranging from 0.2 to 0.7 peak amplitude (Fig. 8, C and H). The mean rise (r) and fall (f) time of the Ca^{2+} puffs were also similar between HEK293 and MCU-KO cells (Fig. 8, D and I), indicating that the fundamental biophysical properties of IP_3R clusters were not different between these two groups of cells. Furthermore, there was no difference between both groups of cells in the proportion of cells that showed a globalized Ca^{2+} signal within 60 s (Fig. 8, E and J). These data suggest that MCU knockout does not alter IP_3R channel activity.

MCU knockout enhances NFAT1/4 activation

Given IP_3R activity is unaltered by MCU-KO, the simplest explanation for enhanced Ca^{2+} oscillations in MCU-KO cells is that MCU-KO causes extramitochondrial Ca^{2+} buildup as mitochondria are unable to buffer their allocated share of cytosolic Ca^{2+} . Hence, cytosol-ER-mitochondrial Ca^{2+} transfer would be backed up in MCU-KO cells, leading to faster ER

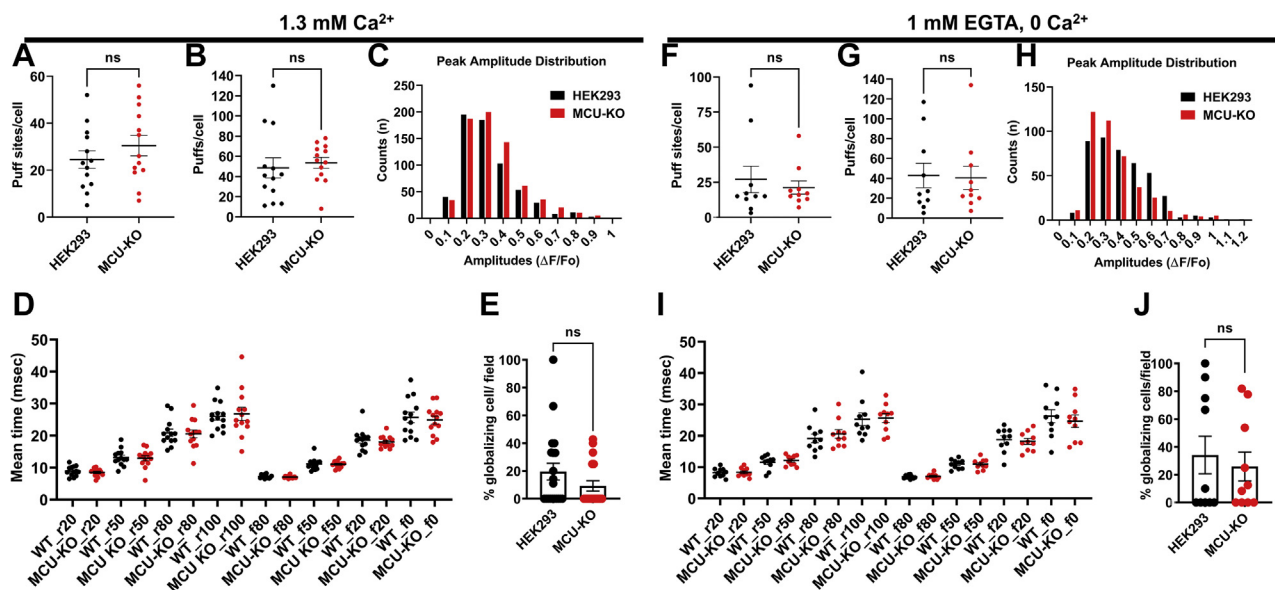


Figure 8. MCU-KO has no effect on inositol-1,4,5-trisphosphate receptor-mediated Ca^{2+} puffs. A–E, Ca^{2+} puffs were measured in Ca^{2+} -containing buffer (1.3 mM Ca^{2+}) using Cal-520 fluorescence ratios ($\Delta\text{F}/\text{F}_0$) from the center of single puff sites ($1.3 \times 1.3 \mu\text{m}$) evoked by photolysis of ci- IP_3 in wildtype HEK293 ($n = 20$ independent experiments; 153 cells) and their MCU-KO counterparts ($n = 19$ independent experiments; 132 cells). A and B, thirteen cells from each condition were randomly selected to quantify the number of puffs (A) and puff sites (B). C, amplitudes distribution of the Ca^{2+} puffs in wildtype HEK293 and MCU-KO cells. D, mean rise and decay times of fluorescence of Ca^{2+} puffs when it increases (r) or decreases (f) to 20%, 50%, 80%, and 100% from 13 cells each of HEK293 and MCU-KO. E, bar graph showing the proportions of wildtype HEK293 and MCU-KO cells in which the calcium signals globalized within 60 s. F–J, similar experiments and data representation to (A–E) in wildtype HEK293 ($n = 11$ independent experiments; 93 cells) and MCU-KO ($n = 12$ independent experiments; 109 cells) where Ca^{2+} puffs were measured in Ca^{2+} -free buffer supplemented with 1 mM EGTA. All data in (A, B, E, F, G, and J) were subjected to an unpaired t test where ns, not significant $p > 0.05$. MCU, mitochondrial Ca^{2+} uniporter.

refilling and/or increased net cytosolic Ca^{2+} . We tested whether the net increase in global cytosolic Ca^{2+} we observed in MCU-KO cells is associated with enhanced NFAT activity, which is controlled by Ca^{2+} microdomains near CRAC channels. NFAT activity was significantly enhanced in MCU-KO cells of both HEK293 (Fig. 9, A–C) and Jurkat cells (Fig. 9, D–F) compared with their respective controls. We determined the effect of MCU-KO on NFAT4 nuclear translocation in HEK293 cells using a reporter NFAT4-GFP construct coupled to fluorescence microscopy (Fig. 9, A–C). In Jurkat cells, we determined the effect of MCU-KO on native NFAT1 nuclear translocation using an NFAT1-specific antibody and ImageStream (Fig. 9, D–F). Stimulation with 10 μ M CCh caused a significantly bigger nuclear translocation of NFAT4 in MCU-KO HEK293 cells when compared with parental controls (Fig. 9, A–C). Using a multispectral imaging flow cytometer (ImageStream) we tracked native NFAT1 nuclear translocation in response to ER store depletion with 2 μ M thapsigargin for 30 min in populations of tens of thousands of MCU-KO Jurkat cells and their parental counterparts. MCU-KO Jurkat cells showed a significantly more robust nuclear translocation of endogenous NFAT1 compared with the parental Jurkat cells (Fig. 9, D–F). These data suggest that the global cytosolic Ca^{2+} increase triggered by deletion of MCU leads to sufficient Ca^{2+} buildup at the

vicinity of CRAC channels to enhance NFAT nuclear translocation.

Tissue-specific MCU knockdown in mice enhances lymphocyte SOCE and proliferation

To determine if the increase in cytosolic Ca^{2+} upon MCU-KO also occurs in primary cells and is not restricted to cell lines, we generated tissue-specific knockdown (KD) mice for $CD4^+$ T cells and B cells (see Fig. S7 for mice genotyping). We used a 4-hydroxytamoxifen (4-OHT)-inducible $CD4$ Cre line to generate mice with $CD4^+$ T cell-specific MCU-KD (Fig. 10, A–G). The B cell-specific MCU-KD mice were generated using the noninducible MB1 Cre line (Fig. 10, H–M). The LoxP-Cre system led to reduction in MCU protein expression by ~60% to 80% (Fig. 10, B–D, H, and I).

Primary $CD4^+$ T cells were isolated with negative selection from spleens of $MCU^{flx/flx}$ mice ($MCU^{flx/flx} CD4^{Cre(-)}$) and $MCU^{flx/flx} CD4^{CreERT2}$ mice ($MCU^{flx/flx} CD4^{Cre(+)}$), activated *in vitro* using anti- $CD3$ /anti- $CD28$ conjugated beads and mouse interleukin-2 (IL-2) and treated with (Z)-4-Hydroxytamoxifen (4-OHT) to induce Cre activity for 96 h before experimentation. Control cells for both $MCU^{flx/flx} CD4^{Cre(+)}$ and $MCU^{flx/flx} CD4^{Cre(-)}$ conditions originated from the same mice but were not subjected to 4-OHT treatment. We verified that the

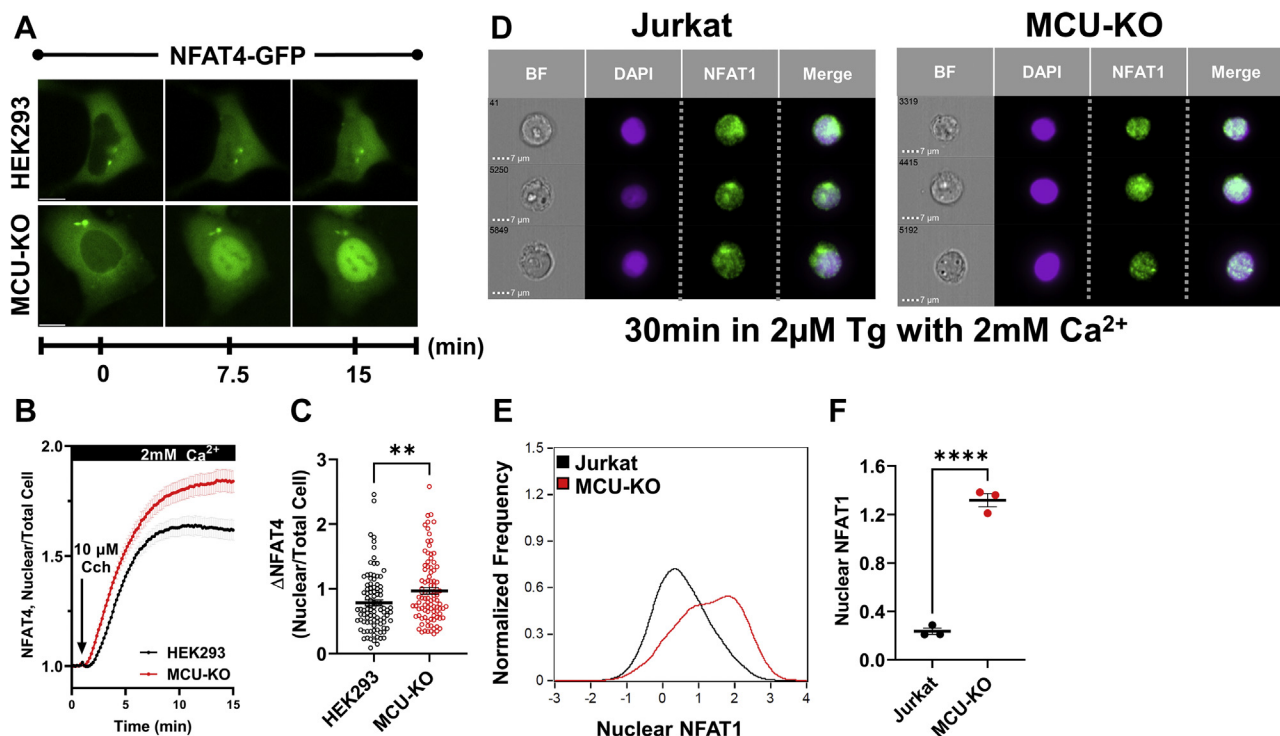


Figure 9. MCU enhances NFAT nuclear translocation. A–C, HEK293 cells and their MCU-KO counterparts were transfected with an NFAT4-GFP construct, stimulated with 10 μ M CCh, and nuclear translocation of NFAT4-GFP was monitored over time using a fluorescence microscope (A; see Experimental procedures, the scale bar represents 10 μ m). The ratio of nuclear/total fluorescence of NFAT4-GFP (B) and difference between maximal and basal ratios (Δ NFAT4; C) are represented for both groups of cells and were statistically analyzed using a Mann–Whitney test where $**p < 0.01$. (D–F), ImageStream analysis of native NFAT1 nuclear translocation using flow cytometry in wildtype and MCU-KO Jurkat cells stimulated with 2 μ M thapsigargin (Tg) for 30 min. Native NFAT1 was labeled with a fluorescently tagged specific antibody, and NFAT1 nuclear translocation was determined by colocalization of NFAT1 with DAPI nuclear staining (D). Histograms showing the distribution (E) and intensity (F) of nuclear NFAT1 fluorescence from $n = 3$ independent experiments with 10,000 cells/run in wildtype Jurkat and MCU-KO cells. The results of these experiments were analyzed using an unpaired t test where $***p < 0.0001$. MCU, mitochondrial Ca^{2+} uniporter; NFAT, nuclear factor for activated T cells.

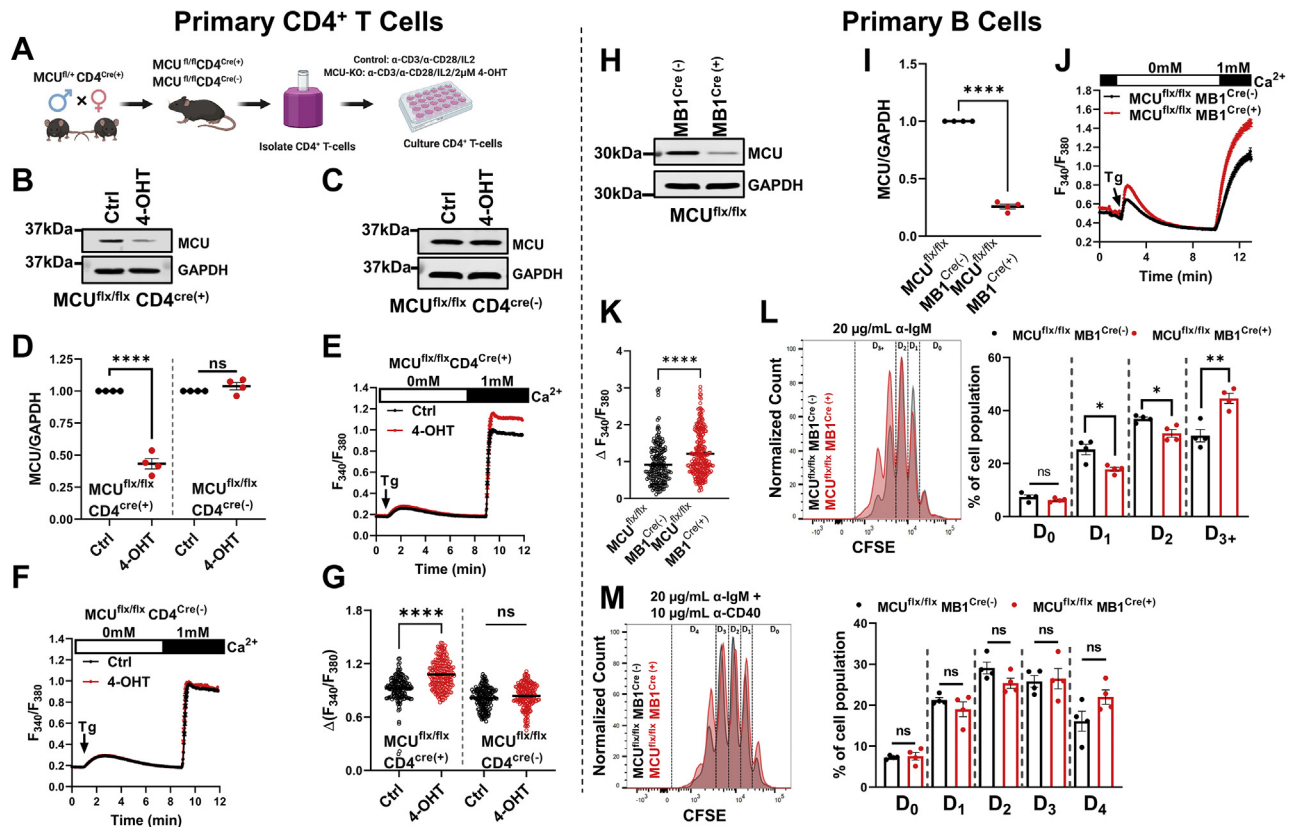


Figure 10. Tissue-specific MCU-knockdown (MCU-KD) in mice $CD4^+$ T and B cells enhances SOCE and proliferation. A–G, primary $CD4^+$ T cells were isolated by negative selection (A) from spleens of $MCU^{fl/fl}; CD4^{Cre(+)}$ and $MCU^{fl/fl}; CD4^{Cre(-)}$ mice identified by genotyping. $CD4^+$ T cell-specific MCU-KD was induced by treating the isolated cells *in vitro* with 4-OHT (B–D). After 4-OHT treatment, only $CD4^+$ T cells from $MCU^{fl/fl}; CD4^{Cre(+)}$ mice show a reduction in MCU protein expression (B and C), which was quantified from $n = 4$ independent mice/group and statistically analyzed using an unpaired *t* test where $****p < 0.0001$ and ns, not significant $p > 0.05$ (D). F and H, Fura2 Ca^{2+} measurements using the SOCE protocol in $CD4^+$ T cells isolated from $MCU^{fl/fl}; CD4^{Cre(+)}$ (E) and $MCU^{fl/fl}; CD4^{Cre(-)}$ (F) mice with and without 4-OHT treatment and maximal SOCE for each group of cells were statistically analyzed (G). H–M, primary B cells were isolated by negative selection from spleens of $MCU^{fl/fl}; MB1^{Cre(+)}$ and $MCU^{fl/fl}; MB1^{Cre(-)}$ mice identified by genotyping. The $MB1^{Cre(+)}$ line is not inducible, and specific MCU-KD was documented on acutely isolated B cells by Westerns (H), and MCU densitometry from four independent isolations was statistically analyzed using an unpaired *t* test where $****p < 0.0001$ and ns, not significant $p > 0.05$ (I). Fura2 Ca^{2+} measurements using the SOCE protocol in B cells isolated from $MCU^{fl/fl}; MB1^{Cre(+)}$ and $MCU^{fl/fl}; MB1^{Cre(-)}$ mice (J) and maximal SOCE for each group of cells was statistically analyzed (K). L and M, B cell proliferation was determined by monitoring the dilution of the CFSE dye with each cell division (D0–D4) using flow cytometry after stimulation with either anti-IgM (L; $n = 4$) or anti-IgM + anti-CD40 (M; $n = 4$). Proliferation data were statistically analyzed using an unpaired *t* test where $*p < 0.05$, $**p < 0.01$, and ns, not significant $p > 0.05$. MCU, mitochondrial Ca^{2+} uniporter; SOCE, store-operated Ca^{2+} entry.

administration of 4-OHT does not alter MCU protein levels in $MCU^{fl/fl}; CD4^{Cre(-)}$ mice (Fig. 10C). Stimulation of cells with 2 μ M thapsigargin showed that only MCU-KD $CD4^+$ T cells, namely, $CD4^+$ T cells isolated from $MCU^{fl/fl}; CD4^{Cre(+)}$ mice and treated with 4-OHT, displayed significantly higher SOCE (Fig. 10, E–G). Because the B cell-specific $MB1^{Cre}$ line is noninducible, primary B cells were isolated with negative selection from spleens of $MCU^{fl/fl}$ mice either with $MB1^{Cre}$ ($MCU^{fl/fl}; MB1^{Cre(+)}$) or without ($MCU^{fl/fl}; MB1^{Cre(-)}$) and immediately used for Ca^{2+} imaging to measure SOCE. Stimulation of B cells with 2 μ M thapsigargin showed that B cells isolated from $MCU^{fl/fl}; MB1^{Cre(+)}$ showed significantly higher SOCE compared with B cells isolated from $MCU^{fl/fl}; MB1^{Cre(-)}$ mice (Fig. 10, J and K).

The induction of MCU-KO with 4-OHT for 5 days in $CD4^+$ T cells from $MCU^{fl/fl}; CD4^{Cre(+)}$ mice precluded us from performing proliferation assays on these primary $CD4^+$ T cells. We did, however, perform proliferation assays on B cells isolated from $MCU^{fl/fl}; MB1^{Cre(+)}$ and $MCU^{fl/fl}; MB1^{Cre(-)}$ mice. B cell proliferation induced by weak B cell receptor

(BCR) stimulation can be enhanced by Ca^{2+} -independent signals such as costimulation with anti-CD40 or stimulation of Toll-like receptors by lipopolysaccharides (LPSs) (40, 41). Therefore, B cells were stimulated *via* their BCR with anti-IgM (Fig. 10L), costimulated with anti-IgM + anti-CD40 (Fig. 10M) or stimulated with LPS alone (Fig. S8C), or stimulated with anti-CD40 alone as a control (Fig. S8D) and B cell proliferation was monitored using the CFSE dye (Fig. S8A). There were no differences in cell viability between different groups of cells and stimulatory conditions (Fig. S8B). Primary B cells from $MCU^{fl/fl}; MB1^{Cre(+)}$ mice (MCU-KD B cells) showed significantly enhanced proliferation in response to BCR stimulation with anti-IgM compared with control $MCU^{fl/fl}; MB1^{Cre(-)}$ B cells as documented by dilution of the CFSE dye with increased proportion of B cells that underwent a third cycle of division (Fig. 10L). As expected, this difference in B cell proliferation was not observed when cells were costimulated with anti-IgM + anti-CD40 (Fig. 10M) or when stimulated with LPS (Fig. S8C). Stimulation with anti-CD40 alone had marginal to no effect on B cell proliferation (Fig. S8D).

Mathematical modeling supports MCU-mediated regulation of cytosolic Ca^{2+}

First, we tested how mitochondrial Ca^{2+} transport alone (*i.e.*, without assuming the existence of microdomains that affect CRAC channel activity through CDI) can change the properties of cytosolic Ca^{2+} rise activated by passive store depletion with thapsigargin as well as Ca^{2+} oscillations activated by agonist stimulation. We took an existing model of Ca^{2+} oscillations (25, 42, 43), slightly simplified the description of the Ca^{2+} influx pathways, and added to it six different models, of increasing complexity, of mitochondrial Ca^{2+} transport.

- Model 1 assumes that mitochondria act like a simple Ca^{2+} buffer, with highly simplified models of Ca^{2+} uptake by the MCU and Ca^{2+} extrusion *via* NCLX.
- Model 2 assumes that the MCU and NCLX fluxes are modeled in a more complex manner, following (44) (itself based on the earlier work of (45, 46)) but omitting the mitochondrial membrane potential and metabolism.
- Model 3 is the same as model 2 but includes the mitochondrial membrane potential and metabolism.
- Model 4 is the model of (44) with no changes to the equations or parameters. It differs from model 3 principally in the choice of IP_3R model and includes models of the mitochondrial membrane potential and metabolism, although it does not include MAMs.

- Model 5 extends model 3 to include MAMs, following (47).
- Model 6 is the model of (47) with no changes to parameters or equations. It differs from model 5 principally in the choice of IP_3R model.

Our six models thus combine in various ways different models of the IP_3R , the mitochondrial potential, mitochondrial metabolism, and MAMs. Model 1 is considerably simpler than the others, whereas models 5 and 6 are the most complex.

When we simulate the effects of MCU-KO, NCLX-KO, and MCU-KO + NCLX-KO on thapsigargin-activated cytosolic Ca^{2+} rise, we found that MCU-KO and MCU-KO + NCLX-KO cause similar increases in cytosolic $[Ca^{2+}]$, whereas NCLX-KO leads to a slight decrease (Fig. 11, A–E), in agreement with our experimental data with MCU and previous work with NCLX (48). This enhancement of cytosolic $[Ca^{2+}]$ upon MCU or NCLX knockout is due simply to the absence of the MCU pathway that removes Ca^{2+} from the cytosol. Ca^{2+} influx to the cytosol remains almost unchanged in the model, but Ca^{2+} removal is downgraded, so an enhancement of cytosolic $[Ca^{2+}]$ necessarily occurs.

These simulations were performed for models 2, 3, and 5 with three variations on model 5 representing different percentages of total IP_3R s located within MAMs (10%, 50%, or 70%; Fig. 11, C–E). These thapsigargin simulations could not be performed for models 1, 4, and 6 as discussed in more detail in [Experimental procedures](#).

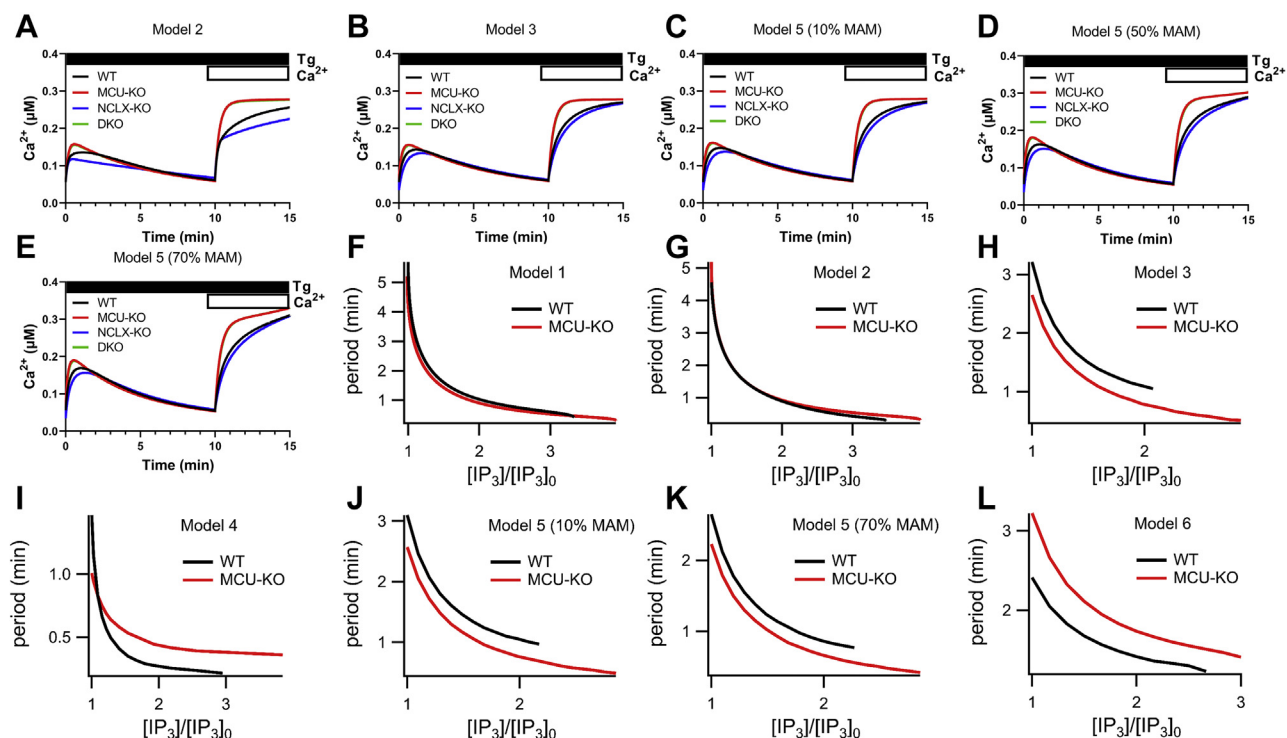


Figure 11. Mathematical modeling shows that MCU-KO increases cytosolic Ca^{2+} but has complex and nonlinear effects on Ca^{2+} oscillations. A–E, various models of the cytosolic Ca^{2+} signal in response to maximal store depletion with Tg in the absence then presence of 2 mM external Ca^{2+} . In model 5, which considers MAM regions of close contact between the endoplasmic reticulum and mitochondria, computations are shown when 10%, 50%, or 70% of total cellular inositol-1,4,5-trisphosphate (IP_3) receptors are located within these MAMs. F–L, period of Ca^{2+} oscillations (1/Frequency) as a function of relative concentrations of IP_3 ($[IP_3]_0$ is the lowest value of $[IP_3]$ for which oscillations exist in the model with MCU) for the six different models described in the [Experimental procedures](#). For model 5, computations are shown when either 10% or 70% of total cellular inositol-1,4,5-trisphosphate receptors are located within the MAMs. MAM, mitochondria-associated membrane; MCU, mitochondrial Ca^{2+} uniporter.

When considering agonist-evoked Ca^{2+} oscillations, the qualitative results from each model differ significantly. For each model, the oscillation period is plotted against the relative $[\text{IP}_3]$, which is a model proxy for agonist stimulation (Fig. 11, *F-L*). In each case, increasing agonist concentration increases the oscillation frequency (*i.e.*, the period decreases). Knockout of the MCU results in oscillations that, in some models, are slightly faster but in others are slightly slower. In some cases (models 2 and 4), the effect on oscillations changes as agonist stimulation increases. Furthermore, in all cases, for a small range of high agonist concentrations, MCU-KO can turn a plateau response into an oscillatory response (this is the region where the red “MCU-KO” curves overlap the black wildtype “WT” curves). It follows that mitochondrial Ca^{2+} transport does not have a simple, monotonic effect on the properties of Ca^{2+} oscillations. Instead, the effects of mitochondrial Ca^{2+} transport are critically dependent on the exact details of each mitochondrial Ca^{2+} flux, as well as other cellular parameters, such as the choice of IP_3R model, the relative mitochondrial volume, or the proportion of the ER membrane that is closely associated with the mitochondrial membrane. In particular, it is not correct to say that “buffering” by the mitochondria will necessarily increase oscillation period; there is no clear relationship between mitochondrial Ca^{2+} transport and oscillation frequency.

Next, we constructed a model that considers MCU activity within a functional I_{CRAC} microdomain (IM model) whereby MCU activity prevents slow CDI of I_{CRAC} . This model also

considers that 10% of IP_3Rs are within MAMs but does not include the equations for mitochondrial metabolism and membrane potential. The inclusion of the mitochondrial metabolism equations makes no qualitative difference to the results. Thus, the IM model is just model 2 with the inclusion of I_{CRAC} CDI and MAMs with all other parameters being unchanged from model 2. We modeled CDI of I_{CRAC} after (34), and initial tests of this IM model gave results that were qualitatively consistent with (34) (Fig. S9). We then simulated the effects of MCU-KO, NCLX-NO, and MCU-KO + NCLX-KO on thapsigargin-activated cytosolic Ca^{2+} rise and agonist-evoked Ca^{2+} oscillations with three variations of this model that consider 10%, 36%, or 70% of the incoming Ca^{2+} through I_{CRAC} enters mitochondria (Fig. 12). The model showed that NCLX-KO leads to a slight decrease in SOCE activated by thapsigargin, whereas MCU-KO and MCU-KO + NCLX-KO cause a similar increase in SOCE that recedes to a lower plateau equivalent to that of wildtype cells. Ca^{2+} oscillations in wildtype and MCU-KO cells in response to increasing concentrations of IP_3 were not altered by 10%, 36% or 70% variations in the IM model (Fig. 12).

In summary, our mathematical modeling predicts that all the experimental results presented here are consistent with the hypothesis that the MCU affects SOCE activated by thapsigargin and Ca^{2+} oscillations evoked by IP_3 -producing agonists only *via* its effect on mitochondrial Ca^{2+} transport, and that no microdomains connected to CRAC channels or IP_3R (MAMs) are required to explain the experimental data.

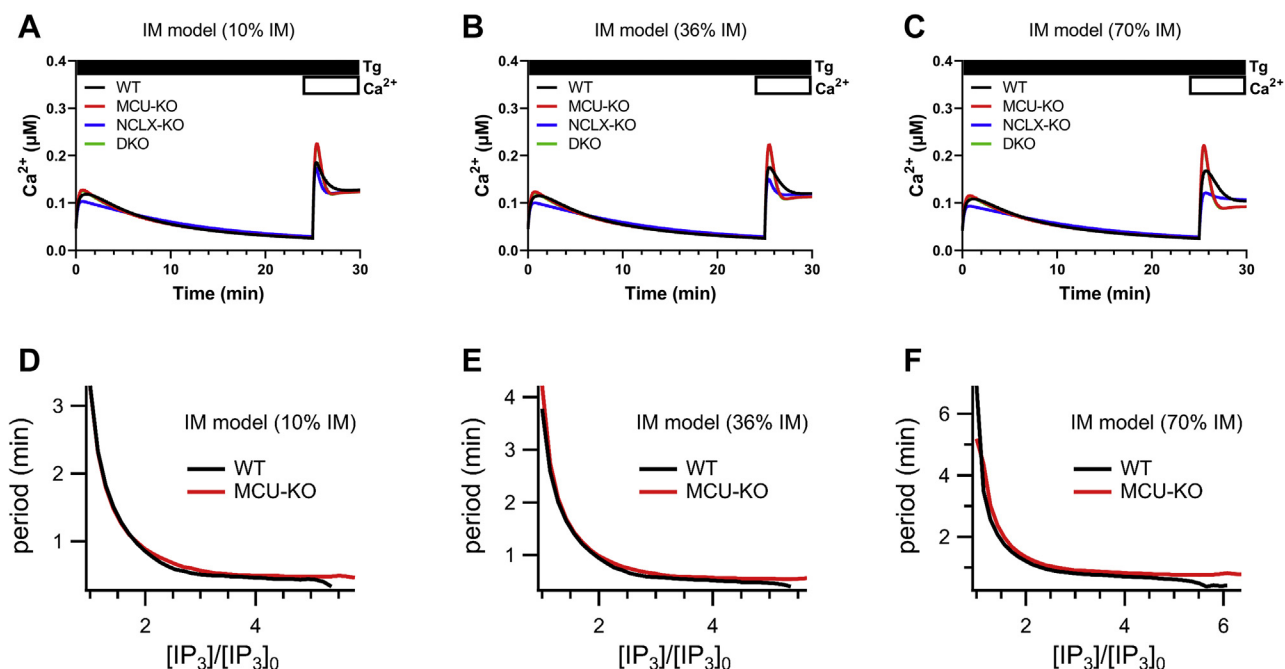


Figure 12. A mathematical model of MCU-KO that also considers I_{CRAC} slow Ca^{2+} -dependent inactivation. Models of I_{CRAC} microdomain (IM) between CRAC and MCU channels whereby slow Ca^{2+} -dependent inactivation of CRAC channels is enhanced in the absence of MCU causing net reduction of I_{CRAC} across the PM. Variations of this model consider that 10%, 36%, or 70% of the incoming Ca^{2+} through I_{CRAC} enters mitochondria. (A–C). Model of the cytosolic Ca^{2+} signal in response to maximal store depletion with thapsigargin in the absence then presence of 2 mM external Ca^{2+} . (E–G). Period of Ca^{2+} oscillations (1/Frequency) as a function of relative concentrations of IP_3 ($[\text{IP}_3]_0$ is the lowest value of $[\text{IP}_3]$ for which oscillations exist in the model with MCU) for the three different IM models from (A–C). CRAC, Ca^{2+} release-activated Ca^{2+} ; IM, I_{CRAC} microdomain; IP_3 , inositol-1,4,5-trisphosphate; MCU, mitochondrial Ca^{2+} uniporter.

Discussion

Through Ca²⁺ uptake and extrusion, mitochondria can shape receptor-activated intracellular Ca²⁺ signaling. Mitochondria rapidly take up Ca²⁺ during receptor-evoked Ca²⁺ signaling and then extrude it much more slowly (49). Mitochondrial Ca²⁺ regulates metabolic activity, through modulation of the activity of three dehydrogenases of the TCA cycle (50, 51). Mitochondria can take up cytosolic Ca²⁺ within the MAM regions of close apposition between IP₃R in the ER and mitochondria (52). In addition, respiring mitochondria can buffer Ca²⁺ from a distant site functionally connected to CRAC channels, thus reducing the extent of slow CDI of these channels to sustain SOCE and cytosolic Ca²⁺ signaling (38, 53).

In this study, we performed genetic knockout of the MCU in several nonexcitable cell lines and in mice to determine the function of MCU in regulating receptor-evoked Ca²⁺ signaling. We reveal that MCU-KO enhances cytosolic Ca²⁺ signaling and downstream activation of NFAT transcription factors. Our data show that store depletion-mediated activation of SOCE and agonist-evoked cytosolic Ca²⁺ oscillations are enhanced when MCU-mediated mitochondrial Ca²⁺ uptake is abrogated. However, this enhancement of cytosolic Ca²⁺ signals is not due to increased activities of either IP₃R or CRAC channels. We measured IP₃R Ca²⁺ puffs in intact MCU-KO and wildtype control cells. The number of IP₃R-mediated Ca²⁺ puffs and number of puff sites were similar between MCU-KO and wildtype cells. We recorded whole-cell CRAC currents from two cell lines under low physiological cytosolic Ca²⁺ buffering conditions with energized mitochondria and under strong cytosolic Ca²⁺ buffering and show that CRAC currents are of similar density in MCU-KO and wildtype parental controls. However, evaluation of CRAC channel slow CDI in the presence of thapsigargin showed that MCU activity prevents store-independent slow CDI of I_{CRAC}, in agreement with previous studies (36, 37). Our data argue that MCU does not alter the activity of native IP₃R. Although MCU function can affect CRAC channel activity by preventing its slow CDI and can inhibit cytosolic Ca²⁺ extrusion, the net result of MCU-KO is an enhancement of cytosolic Ca²⁺ after store depletion or agonist stimulation compared to control cells. Our findings have a simple and straightforward interpretation: abrogation of MCU-mediated Ca²⁺ uptake in response to receptor stimulation prevents the transfer of incoming Ca²⁺ through CRAC channels from the cytosol to mitochondria, causing cytosolic Ca²⁺ accumulation, increased ER Ca²⁺ refilling and enhanced NFAT nuclear translocation.

Using TIRF imaging, Korzeniowski *et al.* (54) showed that on store depletion, mitochondria were remotely distant, or *ad minimum* excluded, from the sites of SOCE, which were visualized by STIM1 puncta and that mitochondrial Ca²⁺ uptake was independent of the distance between STIM1 and mitochondria. Naghdi *et al.* (55) used a mAKAP-RFP-CAAX construct to immobilize mitochondria by linking them to the plasma membrane of endothelial cells and showed that this strategy has no effect on SOCE. Nevertheless, slow CDI of CRAC channels is mediated by a site that is hundreds of nm away, consistent with the reported localization of

mitochondria within ~200nm from Quintana and Hoth (56). Previous studies predating the discovery of MCU showed that abrogation of mitochondrial Ca²⁺ buffering using drugs such as the potent uncoupler of oxidative phosphorylation, FCCP, or the inhibitor of Complex III of the electron transport chain, Antimycin A1, inhibited SOCE (37). This decrease in SOCE resulted, at least partially, from evoking CRAC channel slow CDI (36). Our own findings revealed that mitochondrial depolarization with FCCP indeed inhibits SOCE, in agreement with these studies. However, FCCP equally inhibited SOCE in MCU-KO and wildtype cells, suggesting that, although FCCP promotes I_{CRAC} slow CDI, the drug likely inhibits CRAC channels through additional MCU-independent mechanisms. Because these drugs are known to generate hydrogen peroxide (57, 58), their inhibitory effect on SOCE might be mediated by oxidation of Orai1 (48, 59).

Extensive studies by Hoth and coworkers showed that mitochondria are critical for T cell activation. Upon stimulation, mitochondria move closer to, within 200 nm of, the immune synapse to sequester Ca²⁺. The presence of mitochondria near the immune synapse coincides with enhanced Ca²⁺ concentration near the PM and inhibited cytosolic Ca²⁺ export through the PM Ca²⁺ ATPase, thus enhancing the efficiency of NFAT activity and T cell activation (39, 56, 60, 61). Therefore, both MCU function and its deletion can enhance NFAT activity. The former through inhibition of cytosolic Ca²⁺ export and CRAC channel slows CDI at the PM, whereas the latter through enhanced global cytosolic Ca²⁺. Samanta *et al.* (38) showed blunted SOCE and cytosolic Ca²⁺ oscillations in RBL-1 cells treated with siRNA against MCU and suggested that cytosolic Ca²⁺ uptake by MCU prevents CDI of both IP₃R and CRAC channels. This discrepancy cannot be explained by differences between the MCU knockdown performed by Samanta *et al.* and MCU knockout in our study. We obtained similar results in primary splenic CD4⁺ T cells and B cells isolated from mice subjected to LoxP/Cre-mediated knockdown, which confers ~60% to 80% MCU knockdown as documented by Westerns on isolated CD4⁺ T and B cells. Samanta *et al.* (53) also reported that NCLX knockdown and Na⁺ depletion have no effect on CRAC channels, results that are at odds with previous findings (37, 48). Therefore, the reasons for the discrepancy between the studies by Samanta *et al.* and ours are not clear. However, these investigators reported results from a single cell line, used one single siRNA, did not document protein or mRNA knockdown of MCU or NCLX, and did not rule out off-target effects on STIM–Orai expression in their system (38, 53).

Although NFAT nuclear translocation is driven by Ca²⁺/CaM-dependent activation of calcineurin at the vicinity of CRAC channels, NFAT activity also depends on other signaling regulators, including several kinases that differentially regulate the nuclear export of various NFAT isoforms (62). We cannot exclude the possibility that other mechanisms of NFAT regulation are altered in MCU-KO cells and further studies are required to further clarify this issue. We show that B cells isolated from B cell-specific MCU

knockdown mice have enhanced proliferation compared with B cells isolated from littermate controls. However, previous studies in HeLa cells and vascular smooth muscle cells showed that MCU knockdown or knockout halts cell cycle progression and reduces proliferation (63, 64). The discrepancy between these previous studies and ours can likely be explained by the differential requirement for MCU by cancer cells and proliferative smooth muscle cells *versus* B cells. The contribution of mitochondrial Ca^{2+} to bioenergetics in cancer cells and proliferative smooth muscle cells is likely more prominent than in hematopoietic cells, which rely heavily on glycolysis. The effect of MCU-KO on enhanced NFAT activity in cancer cells and proliferative smooth muscle cells is likely largely offset by the disruption of mitochondrial metabolism as a result of MCU loss.

Our mathematical modeling support previous computational work showing that the effects of mitochondrial Ca^{2+} transport on cytosolic Ca^{2+} oscillations are complex and nonintuitive (65). Although mitochondria take up and release cytosolic Ca^{2+} in a manner superficially similar to that of a traditional Ca^{2+} buffer, the complexities and nonlinearities inherent to these transport processes mean that the downstream effects on oscillation frequency cannot be easily predicted. In some cases, oscillation frequency is increased by mitochondrial transport; in other cases, oscillation frequency is decreased. Thus, the common understanding that inhibition of mitochondrial Ca^{2+} buffering decreases oscillation frequency is not supported by our modeling. Our models showed that MCU-KO enhances, whereas NCLX-KO decreases, cytosolic Ca^{2+} rise in response to store depletion by thapsigargin. Our modeling predicts that MCU-KO mediates its effects only through changes in mitochondrial Ca^{2+} transport and that no Ca^{2+} microdomains that can alter CDI of Ca^{2+} channels (CRAC or IP_3R) are required to explain our experimental data. Ishii *et al.* (66) showed that, during Ca^{2+} oscillations in HeLa cells Ca^{2+} shuttles between the ER and mitochondria and that Ca^{2+} uptake by mitochondria occurs at the expense of refilling of the ER, in agreement with our observations. Our model of NCLX-KO is also consistent with previous experimental findings from our group and others. Hoth *et al.* (37) showed that SOCE was reduced when NCLX was inhibited in cells subjected to Na^+ depletion and Naghdi *et al.* (55) showed reduction in SOCE when cells were treated with CGP37157, a pharmacological inhibitor of the NCLX. We previously reported that molecular knockdown of NCLX or Na^+ depletion inhibits SOCE and CRAC channel activity in HEK293 cells and primary vascular smooth muscle cells (48).

In summary, in addition to preventing CRAC channel inactivation and inhibiting cytosolic Ca^{2+} extrusion to enhance NFAT activity, mitochondrial Ca^{2+} uptake by MCU and Ca^{2+} storage by mitochondria is concomitantly critical for negative regulation of cytosolic Ca^{2+} and NFAT induction. These two concomitant and reciprocal functions of MCU at the cytosol–mitochondria interface fine-tune interorganellar Ca^{2+} transfer and NFAT activation during receptor-evoked signaling.

Experimental procedures

Cell culture

Parental HEK293, Jurkat E6-1, RBL-1, DLD1, HCT116, and A20 cell lines were purchased directly from ATCC (Catalog # CRL-1573, TIB-152, CRL-1378, CCL-221, CCL-247, and TIB-208). HEK293, RBL-1, and HeLa cells were cultured in high-glucose (4.5 g/l) Dulbecco's modified Eagle's medium supplemented with 10% heat-inactivated fetal bovine serum and 1× Antibiotic–Antimycotic solution. Jurkat, A20, and DLD1 were maintained in RPMI 1640 with L-glutamine supplemented with 10% heat-inactivated fetal bovine serum and 1× Antibiotic–Antimycotic solution. HCT116 were cultured in McCoys 5A medium supplemented with 10% heat-inactivated fetal bovine serum and 1× Antibiotic–Antimycotic solution. All cell lines were stored in a heated (37 °C) humidified incubator under standard cell culture conditions (5% CO_2 ; 95% air). The absence of mycoplasma contamination was verified for all cell lines using a sensitive PCR-based detection kit (ABM: G238).

Fluorescence imaging

Adherent and semiadherent cell lines were seeded onto round 25-mm glass coverslips 24 h prior to imaging at a concentration of 1.5×10^6 and 2.5×10^6 cells, respectively. Alternatively, A20, Jurkat E6-1, and primary CD4^+ T cells were seeded onto round Poly-L-lysine (0.01%; mol wt 150,000–300,000)-treated 25-mm glass coverslips 30 min prior to dye loading. Once attached, HEK293, HeLa, HCT116, and DLD1 cells were incubated in Dulbecco's modified Eagle's medium containing the ratiometric Ca^{2+} indicator Fura-2 AM (2 μM) for 30 min. RBL-1 cells were loaded with 4 μM Fura-2AM following the same procedure. Jurkat and A20 cells were incubated with 2 μM Fura-2 AM in HEPES-buffered salt solution (HBSS; 120 mM NaCl, 5.4 mM KCl, 0.8 mM MgCl_2 , 20 mM HEPES, 10 mM glucose adjusted to pH 7.4 with NaOH) supplemented with 2 mM Ca^{2+} for 30 min at room temperature. Before imaging, all coverslips were transferred from a standard six-well plate into an Attotfluor cell chamber and washed 3× with Ca^{2+} -containing HBSS to remove excess Fura-2 AM. Using a fast shutter wheel (Sutter Instruments), cytosolic Ca^{2+} was measured by alternatively exciting Fura-2 with 340- and 380-nm wavelengths and recording the resulting 510-nm dye emission on a pixel-by-pixel basis through a 20× fluorescence objective paired with a Hamamatsu Flash 4 camera and processed using Leica Application Suite X software.

Measurement of NFAT4 nuclear translocation in HEK293 cells was achieved by transient overexpression of NFAT4-GFP (Addgene #21664) as previously described (32, 42, 43). Briefly, 1×10^6 cells were incubated with a solution containing 1 μg of NFAT4-GFP and 3 μl Lipofectamine 2000 for 3 h. One day later, coverslips containing transfected cells were transferred to imaging chambers and washed with Ca^{2+} -containing HBSS as described above. Using a Leica imaging system and a 40× oil immersion objective, NFAT4-GFP was excited at 488 nm, and emission spectra were selectively captured through a GFP filter

cube. Real-time analysis of NFAT4-GFP nuclear translocation in response to 10 μM Cch stimulation was calculated using the equation:

$$NFAT4 \text{ Translocation} = \left(\frac{Nuclear_{F510}}{Whole \text{ Cell}_{F510}} \right)$$

Quantification of ER Ca²⁺ store depletion and refilling was done by transfecting parental and MCU-KO HEK293 cells with red R-CEPIA1er (Addgene: #58216) using Lipofectamine 24 h prior to imaging. Cells expressing R-CEPIA1er were then excited at 552 nm and relative ER Ca²⁺ measurements recorded through a 40× oil immersion objective. Immediately after identifying R-CEPIA1er-positive cells the bath solution was replaced with nominally Ca²⁺-free HBSS. One minute into the experiment cells were treated with CCh followed by washout and readdition of 2 mM Ca²⁺ to the bath. The resulting traces represent ±SEM of all cells from at least three independent experiments.

Ca²⁺ puff measurements using TIRF microscopy

Parental WT-HEK293 cells or MCU-KO cells were grown on 15-mm glass coverslips coated with poly-D-lysine (100 μg/ml) in a 35-mm dish for 2 days and imaged as described (42). Prior to imaging, the cells were washed three times with imaging buffer (137 mM NaCl, 5.5 mM glucose, 0.56 mM MgCl₂, 4.7 mM KCl, 1.26 mM CaCl₂, 10 mM Hepes, 1 mM Na₂HPO₄ at pH 7.4). Cells were subsequently incubated with Cal520-AM (5 μM; AAT Bioquest #21130) and 6-O-[(4,5-Dimethoxy-2-nitrophenyl)methyl]-2,3-O-(1-methylethylidene)-D-*myo*-Inositol 1,4,5-tris[bis[(1-oxopropoxy)methyl]phosphate] (ci-IP₃/PM; 1 μM, Tocris #6210) in imaging buffer with 0.01% bovine serum albumin in dark at room temperature. One hour later, cells were washed three times with imaging buffer and incubated in imaging buffer containing EGTA-AM (5 μM, Invitrogen #E1219). After 45 min incubation, the medium was replaced with fresh imaging buffer and incubated for an additional 30 min at room temperature to allow for de-esterification of loaded reagents (67).

Following loading, the coverslip was mounted on chambers and imaged using an Olympus IX83 inverted TIRF microscopy equipped with oil immersion Olympus UPLAPO60XOHR (NA = 1.5) objective. The cells were illuminated using a 488-nm laser to excite Cal-520, and the emitted fluorescence was collected through a band-pass filter by a Hamamatsu ORCA-Fusion CMOS camera. The angle of the excitation beam was adjusted to achieve TIRF with a penetration depth of ~140 nm. Images were captured from a field of view by directly streaming into RAM. To photorelease IP₃, UV light from a 405-nm laser at 50% power was introduced to uniformly illuminate the field of view. Both the intensity of the UV flash (~2.4 mW) and the duration (1000 ms) for uncaging IP₃ were optimized to prevent spontaneous puff activity in the absence of loaded ci-IP₃. TIRF images were captured using 4 × 4 pixel binning (433.333 nm/pixel) from equal field of views for WT-HEK293 and MCU-KO cells at a rate of ~166 frames per

second. After visualizing images with the cellSens [Ver.2.3] life science imaging software (Olympus), images were exported as vsi files. Images, 10 s before and 60 s after flash photolysis of ci-IP₃, were captured.

The vsi files were converted to tif files using Fiji and further processed using FLIKA, a Python programming-based tool for image processing (68). From each recording, 500 frames (~3 s) before photolysis of ci-IP₃ were averaged to obtain a ratio image stack (F/F₀) and standard deviation for each pixel for recording up to 20 s following photolysis. The image stack was Gaussian filtered, and pixel that exceeded a critical value (1.0 for our analysis) was located. The “Detect-puffs” plug-in was utilized to detect the number of clusters (puff sites), number of events (number of puffs), amplitudes, and durations of localized Ca²⁺ signals from individual cells. All the puffs identified automatically by the algorithm were manually confirmed before analysis (69, 70). The results from FLIKA were saved as excel, and graphs were plotted using GraphPad Prism8.

Patch clamp electrophysiology

RBL-1 cells were seeded onto 30-mm round glass coverslips 12 h before recording; Jurkat cells were seeded onto Poly-L-lysine-coated coverslips 1 h before recording. Native I_{CRAC} recordings were carried out using an Axopatch 200B and Digidata 1440A (71–73). Pipettes were pulled from borosilicate glass capillaries (World Precision Instruments) with a P-100 flaming/brown micropipette puller (Sutter Instrument Company) and polished with DMF1000 (World Precision Instruments). Resistances of filled glass pipettes were 2 to 4 MΩ. Only cells with tight seals (>16 GΩ) were selected for break-in. Cells were maintained at a +30-mV holding potential during experiments and subjected to 250-ms voltage ramps from 100 to -140 mV every 3 s. Reverse ramps were designed to inhibit Na⁺ channels potentially expressed in these cells. All experiments were performed at room temperature. MgCl₂, 8 mM, was included in the pipette solution to inhibit TRPM7 currents. CRAC currents were induced by either 30 μM inositol-1,4,5-trisphosphate (1,4,5-IP₃) or 50 mM BAPTA. Clampfit 10.3 software was used for data analysis. The solutions employed for patch clamp recordings are as follows.

Bath solution:

115 mM Na-methanesulfonate, 10 mM CsCl, 1.2 mM MgSO₄, 10 mM Hepes, 20 mM CaCl₂, and 10 mM glucose (pH 7.4, adjusted with NaOH).

Divalent-free bath solution:

155 mM Na-methanesulfonate, 10 mM HEDTA, 1 mM EDTA, and 10 mM Hepes (pH 7.4, adjusted with NaOH).

Pipette solution 1 (low buffer):

135 mM Cs-methanesulfonate, 1 mM EGTA, 8 mM MgCl₂, and 10 mM Hepes, 0.03 mM IP₃, 2 mM pyruvic acid, 2 mM malic acid, 1 mM NaH₂PO₄, 2 mM Mg-ATP (pH 7.2 adjusted with CsOH).

Pipette solution 2 (high buffer):

85 mM Cs-methanesulfonate, 50 mM Cs-1,2-bis-(2-aminophenoxy)ethane-N,N',N',N'-tetraacetic acid (Cs-BAPTA), 8 mM MgCl₂, and 10 mM Hepes (pH adjusted to 7.2 with CsOH).

Recordings of CRAC channel store-independent slow CDI were performed according to (36). Cells were incubated in the bath solution without Ca²⁺ and in the presence of 2 μM thapsigargin for 3 to 5 min before beginning of recordings. The bath and pipette solutions were as follows:

Bath solutions:

0 mM Ca²⁺ bath solution (in mM): 155 NaCl, 4.5 KCl, 3 MgCl₂, 10 D-glucose, and 5 Hepes (pH = 7.4 with NaOH).
20 mM Ca²⁺ bath solution (in mM): 125 NaCl, 4.5 KCl, 20 CaCl₂, 3 MgCl₂, 10 D-glucose, and 5 Hepes (pH = 7.4 with NaOH).

Pipette solutions:

Low buffer pipette solution (in mM): 140 Cs-methanesulfonate, 2 MgCl₂, 0.66 CaCl₂, 1.2 EGTA, 10 Hepes (pH = 7.2 with CsOH).

Low buffer + mitochondrial cocktail pipette solution (in mM): 140 Cs-methanesulfonate, 2 MgCl₂, 0.66 CaCl₂, 1.2 EGTA, 10 Hepes, 2.5 mM malic acid, 2.5 mM pyruvate acid, 1 mM NaH₂PO₄, 5 mM Mg-ATP, 0.5 mM Na-GTP (pH = 7.2 with CsOH).

Cytosolic and mitochondrial volume determination

To determine the cytosolic volume of all cell lines pEGFP-N1 (Addgene# 6085-1) was transiently overexpressed. One day before cytosolic volume measurement all cell lines were electroporated using the Amaxa Nucleofector II. Cells were first resuspended in the transfection reagent supplemented with pEGFP-N1 (1 μg). Cell line-specific protocols Q-001, X-001, T-030, and L-013 were used to electroporate HEK293, Jurkat, RBL-1, and A20 cells, respectively. One day later, live cells were stained with MitoTracker Deep Red (200 nM) for 15 min at room temperature in the dark before imaging on a Leica DMI8 confocal microscope. Stained and washed cells were observed through a 40× oil immersion objective. Both GFP and MitoTracker signals were then collected from randomly selected fields of view by compiling Z-Stacks of the lower and upper bounds of all cells. MitoTracker and GFP channels were then used to reconstruct 3D surfaces using IMARIS Cell Biology software (Oxford Instruments). Once both cytosolic (GFP) and mitochondrial (MitoTracker) surfaces were reconstructed, volume measurements were recorded individually.

ImageStream native NFAT1 nuclear translocation assay

Jurkat cells were first counted and transferred to 1.5-ml Eppendorf tubes at a concentration of 1.2 × 10⁶ cells per replicate. Cells were then centrifuged and media replaced with HBSS supplemented with 2 mM Ca²⁺ to eliminate the possibility of serum-mediated activation. Experimental cells were then

stimulated with α-CD3 (0.125 μg/ml) or treated with Tg (2 μM) to induce cytosolic Ca²⁺ oscillations or evoke SOCE. Following stimulation, cells were immediately fixed and permeabilized using a transcription factor staining kit according to the manufacturer protocol (Tonbo Biosciences Cat: TNB-0607-KIT). After fixation and permeabilization, cells were spun down, the supernatant was removed, and stained with a primary conjugated NFAT1-FITC antibody (Cell Signaling #14324S at 1:100) for 1 h at room temperature protected from light. Unbound NFAT1 antibody was then washed away and cells were resuspended in 40 μL of PBS. Nuclear staining was performed immediately before image acquisition by adding 10 μL of the nuclear stain Dapi (5×) to give a final concentration of (0.25 μg/ml).

Images were acquired using a 10-color Amnis ImageStream X Mk II imaging cytometer. Channels 1 and 9 (430–480 nm) were used to obtain bright-field images, channel 2 was used for FITC (Ex:488 Em:480–560 nm), and Dapi through channel 7 (Ex:405 Em:430–505 nm). Prior to final image acquisition cells were gated to exclude debris and doublets and Ex laser power was adjusted to prevent pixel saturation. From each stained and unstained sample 3000 to 5000 in-focus single-cell events were collected. After running all samples single color compensation samples were run for FITC then Dapi. All data were analyzed using IDEAS software version 6.2 (Amnis Corp). During the analysis in-focus cells were first identified, then doublets were excluded, and finally cells positive for both DAPI and NFAT1 were selected for further analysis. The extent of nuclear NFAT1 was then determined using the nuclear translocation module. Raw nuclear similarity scores were then exported to Prism GraphPad resulting in the final figures.

Generation of transgenic MCU^{fl/fl} CD4^{Cre(Ert2)} and MCU^{fl/fl} MB1^{Cre} mice

We generated inducible MCU-KO CD4⁺ T cells by breeding MCU^{flx/flx} mice (generous gift from Dr John W. Elrod, Temple University) (74) with CD4CreER^{T2} (B6(129X1)-Tg(Cd4-cre/ERT2)11Gnri/J) purchased from Jackson laboratory (75). The resulting CD4CreER^{T2}-positive MCU^{fl/wt} mice from this cross were then bred with MCU^{fl/fl} mice to generate all control and experimental cohorts. B cell-specific knockout of MCU was achieved by breeding MB1-Cre (B6.C(Cg)-Cd79a^{tm1(cre)Reth/EhobJ}) mice from Jackson laboratory with MCU^{fl/fl} mice. From that cross MCU^{fl/wt}MB1Cre^{+/-} were then bred with MCU^{fl/fl} mice to generate the experimental and control groups (76). PCR-based genotyping was performed on all mice to identify experimental and control mice. Western blots were used to validate MCU-KO at the protein level. Both male and female mice were utilized in equal numbers to reduce the possibility of sex-dependent variation biasing the results. All mice were maintained in the specific pathogen-free barrier animal facility at the Pennsylvania State University College of Medicine animal facility. Prior to any breeding or experimentation all protocols used were approved by the Pennsylvania State Institutional Animal Care and Research Advisory Committee (IACUC) to ensure all animals were handled and cared for according to ethical guidelines.

Primary T and B cell isolation and culture

About 6 to 8-week-old MCU^{fl/fl} CD4^{Cre+} or MCU^{fl/fl} MB1^{Cre+} mice and control counterparts were humanely sacrificed immediately prior to immune cell isolation. Superficial cervical and inguinal lymph nodes were first collected followed by the spleen. All lymphoid tissues were then disrupted by passing the tissue through a 70- μ m mesh screen. The resulting single-cell suspension was then washed with 10 ml of cold RPMI and resuspended in 1 ml of Robosep buffer (STEMCELL technologies) prior to the negative selection of B or T cells. Using the corresponding negative selection kit primary mouse CD4⁺ T cells and B cells were isolated using the magnetic beads and antibody cocktail as recommended by the manufacturer.

Isolated CD4⁺ T cells were then cultured *ex vivo* to increase the efficiency of CRE^{ERT2} activity. Naïve primary CD4⁺ T cells were maintained in RPMI 1640 supplemented with 10% fetal bovine serum, 1 \times Antibiotic-Antimycotic, 1 \times Glutamax, mIL2 (30 U/ml), and Mouse T-Activator anti-CD3/CD28 Dynabeads (Thermo Fisher) at a concentration of one bead per cell. Experimental mice (MCU^{fl/fl} CD4^{Cre+}) and control (MCU^{fl/fl} CD4^{Cre-}) mice were both treated with 2 μ M 4-OHT for 4 days. As a control, the second group of (MCU^{fl/fl} CD4^{Cre-}) mice was only administered vehicle (dimethyl sulfoxide). Cells were subsequently washed and beads removed.

Genetic knockout of MCU in multiple cell lines using CRISPR/Cas9

To generate MCU-KO HEK293 and HCT116 cells, human MCU gRNA3 (hMCU gRNA1) was subcloned into the lenti-CRISPR v2 backbone (Addgene, Plasmid #52961) and transfected into wildtype HEK293 cells *via* nucleofection as described. Forty-eight hours after transfection, CRISPR/Cas9-positive cells were selected by treating the culture medium with puromycin (2 μ g/ml) (Gemini Bio Products). After 6 days of selection, cells were trypsinized and seeded at a concentration of 0.5 cells per well into a 96-well plate. Resulting colonies were then screened using the Guide-it Mutation Detection Kit (Clontech Laboratories, 631443). Knockout was further confirmed *via* Western blot, functional analysis, and genomic sequencing.

An alternative method was used for all other cell lines to avoid any potential effects of constitutive Cas9 expression. The same two human gRNAs (hMCU gRNA1 and 2) were used to generate all Jurkat and DLD1 MCU-KO clones. Two independent mouse-specific gRNAs (mMCU gRNA 1 and 2) were used to generate MCU-KO A20 cells, whereas a single gRNA (rMCU gRNA1) was used to generate MCU-KO RBL-1 cells. All gRNA sequences can be found in [Table S1](#).

gRNAs for all cell lines were cloned into one of two fluorescent vectors to allow for the identification of transiently transfected cells using fluorescence-activated cell sorting (pSpCas9(BB)-2A-GFP and pU6-(BbsI)_CBh-Cas9-T2A-mCherry; Addgene). One day after transfection with the corresponding gRNA single cells with high gRNA expression were sorted into the wells of a 96-well plate using a fluorescence-activated cell sorting Aria SORP high-performance cell

sorter. After sorting, cells were maintained in complete medium until colonies began to form \sim 2 to 3 weeks depending on the cell line. Visible colonies were collected and analyzed by Western blot to identify knockout clones. Positive clones were functionally analyzed, and those clones that showed no mitochondrial Ca²⁺ uptake were used for all experiments.

Furthermore, all clones were sequenced to validate gRNA efficiency. In HEK293 MCU-KO cells we observed two different genomic deletions (11 and 1 nt; exon 2) that resulted in a genomic frameshift and the formation of early stop codons. In Jurkat MCU-KO cells we also observed two different mutations. The first was a 7-nt insertion into exon 3, and the second caused multiple indels that resulted in a genetic frameshift and formation of an early stop codon in exon 3. In RBL-1 we observed two different deletions from exon 3 (16 and 400 nt) that both resulted in genomic frameshifts. Two different deletion events were also observed in A20 cells; the first was a single-nucleotide deletion and the second a 7-nt deletion from exon 1. We also observed two different deletions in HCT116, the first being a 16-nt deletion and the second a 19-nt deletion; both occurred in exon2 and resulted in frameshifts. In DLD1 cells, two unique 2-nt deletions were observed within exon 4 that both resulted in genomic frameshifts and the introduction of an early stop codon.

Western blot analysis

Cells were collected from culture flasks or isolated from mice, washed with ice-cold phosphate-buffered saline, and pelleted *via* centrifugation prior to lysis in ice-cold RIPA buffer (150 mM NaCl, 1.0% IGEPAL CA-630, 0.5% sodium deoxycholate, 0.1% SDS, 50 mM Tris pH 8.0; Sigma) supplemented with protease and phosphatase inhibitor (Halt; Thermo Scientific) for 15 min on ice. Crude protein lysates were clarified by centrifugation (15,000g/12 min at 4 °C) and the supernatants collected. Total protein concentration was determined using the Pierce BCA assay as described prior to loading a NuPAGE precast 4% to 12% Bis-Tris gel. After subjecting the samples to 120 V for 1.5 h proteins were transferred to a polyvinylidene difluoride membrane using a Bio-Rad Criterion blotter and 1 \times NuPAGE Transfer Buffer (Invitrogen). After 1 h of transferring at 95 V the membrane was removed and blocked with LI-COR Tris-buffered saline (TBS) buffer for 1 h at room temperature. Primary antibodies were added to blocked membranes overnight at 4 °C in a shaker. On the next day, PVDF membranes were then washed 3 \times with TBST and probed with the corresponding species-specific LI-COR secondary antibody for 1 h at room temperature. Then the membrane was washed 3 \times with TBST and immediately imaged using a LI-COR odyssey imaging system and fluorescence quantified using Image Studio lite software (LI-COR).

Measurement of mt Ψ and mtCa²⁺ uptake in permeabilized cells

HEK293 (6×10^6), Jurkat (10×10^6), A20 (10×10^6), and RBL-1 (7×10^6) cells were washed with PBS immediately

before resuspension in an intracellular medium consisting of 10 mM NaCl, 120 mM KCl, 1 mM KH₂PO₄, 20 mM Hepes-Tris, pH 7.2, and 2 μM of the SERCA pump inhibitor thapsigargin. Just before beginning the measurement 2 mM succinate was added to the intracellular medium. Cells were permeabilized with 40 μg/ml digitonin, and simultaneous measurements of mitochondrial membrane potential (mtΨ) and extramitochondrial Ca²⁺ were achieved by loading permeabilized cells with the ratiometric mtΨ dye JC-1 (800 nM) and the fluorescent Ca²⁺ indicator Fura2-FF (0.5 μM). Both dyes were excited, and emissions were recorded using a dual-wavelength excitation and emission fluorimeter (Delta Ram, PTI).

qRT-PCR analysis

Total mRNA was isolated from HEK293 (2 × 10⁶) and Jurkat cells (4 × 10⁶) parental and MCU-KO cell lines using the RNeasy Mini Kit (Qiagen). Isolated RNA was then analyzed using a NanoDrop spectrophotometer (Thermo Scientific), and 1 μg of DNase I-treated (Thermo Fisher) RNA was reverse transcribed using the High-Capacity cDNA Reverse Transcription Kit (Applied Biosystems). Total cDNA (1 μl) was diluted 1:5 and then combined with target-specific primers, SYBR Green qPCR Master Mix (Applied Biosystems), and mqH₂O resulting in a 10-μl total reaction. All targets were subjected to the same PCR protocol that began with an initial activation step for 2 min at 50 °C followed by a 95 °C for 2 min melt step. The initial melt steps were then followed by 40 cycles of 95 °C for 15 s, a 15-s annealing step at 54.3 °C, and target amplification at 72 °C for 30 s. Once these steps were complete, a standard melt curve was generated to ensure primer specificity. Analysis of target and control samples was carried out using the comparative Ct method. All samples were normalized to the average of the two reference genes, GAPDH (glyceraldehyde-3-phosphate dehydrogenase) and NONO (Non-POU Domain Containing Octamer Binding). All samples were run in triplicate to ensure reproducibility.

Mathematical modeling

Models of the IP₃R, SERCA, and the PM ATPase were taken directly from (42, 43), with unchanged parameters. The model of Ca²⁺ influx, however, was simplified from that of (42, 43) by omitting the majority of the complexity generated by two different forms of STIM and three different forms of ORAI. Instead, we modelled Ca²⁺ influx by

$$J_{in} = A \left(1 - \frac{(1-1/v_1)c_e^8}{K_{e1}^8 + c_e^8} \right) \left(1 - \frac{c_e^8}{K_{e2}^8 + c_e^8} \right) + \alpha_0,$$

where A = 0.2 μM/s, v₁ = 3, K_{e1} = 50 μM, K_{e2} = 200 μM, and α₀ = 0.005 μM/s. The variable c_e denotes ER [Ca²⁺].

To incorporate mitochondrial transport, the base model was supplemented by the addition of three terms each representing a mitochondrial Ca²⁺ flux: a flux through the MCU (J_{MCU}), a

flux through the NCLX (J_{NCLX}), and (following (44)) a background leak term (J_x). The four different models of mitochondrial Ca²⁺ transport are as follows.

Model 1. The mitochondria are modeled as simple buffers. Thus

$$J_{MCU} = k_{on}c(b_t - c_m),$$

$$J_{NCLX} = k_{off}c_m,$$

$$J_x = 0,$$

where k_{on} = 3 μM⁻¹s⁻¹, k_{off} = 5/s, b_t = 5 μM were chosen so as to give a physiological resting value of c_m and to ensure that the buffering was close to linear. The variable c_m denotes the mitochondrial [Ca²⁺].

Model 2. The mitochondrial fluxes are modeled following (44) but with the omission of the mitochondrial membrane potential and the mitochondrial metabolism. Thus

$$J_{MCU} = V_{MCU} \frac{\phi_1}{\phi_2},$$

$$\phi_1 = \left(\frac{c}{K_1} \right) \left(1 + \left(\frac{c}{K_1} \right)^3 \right),$$

$$\phi_2 = \left(1 + \left(\frac{c}{K_1} \right)^4 \right) + \frac{L}{1 + (c/K_2)^{2.8}},$$

$$J_{NCLX} = V_{NCLX}(c_m / c),$$

$$J_x = k_x(c - c_m),$$

where V_{MCU} = 15 μM/s, K₁ = 6 μM, K₂ = 0.38 μM, V_{NCLX} = 0.005 μM/s, L = 50, and k_x = 0.01/s. The variable c denotes the cytosolic [Ca²⁺].

Model 3. The mitochondrial fluxes are modeled following (44) (and use the same parameter values), including the mitochondrial membrane potential and the equations describing mitochondrial metabolism. As with the previous models, the model of the IP₃R is taken from (25, 42, 43), and thus the results from model 3 are not identical to those of (44). No MAM microdomains are included.

Model 4 is identical to the model of (44).

Model 5. The mitochondrial fluxes are identical to those of model 3, but now MAMs are included, in the manner of (47) (*i.e.*, using a compartmental model approach and not including any spatially distributed compartments). However, the IP₃R model is the same as in model 3, and thus models 5 and 6 give

significantly different outcomes. To maintain a physiological resting c_m , V_{MCU} was increased to 150 $\mu\text{M/s}$.

Model 6 is identical to the model of (47).

Model for calcium-dependent inactivation of I_{CRAC}

A specified fraction (10%, 36%, or 90%) of J_{in} was assumed to enter the cell directly into an IM formed between the PM and the mitochondrial membrane, containing only I_{CRAC} and MCU. Inclusion of NCLX and/or PM Ca²⁺ pumps into the IM makes no qualitative difference to the results. To describe calcium-dependent and time-dependent inactivation of I_{CRAC} we used one of the simplest possible models. A new time-dependent variable, h_{icrac} , was introduced, obeying the differential equation

$$\tau_{icrac} \frac{dh_{icrac}}{dt} = h_{icrac,\infty} - h_{icrac},$$

where

$$h_{icrac,\infty} = \frac{K_{icrac}^2}{K_{icrac}^2 + x^2}.$$

Here, x is either the cytosolic or IM $[\text{Ca}^{2+}]$ depending on whether we are modeling the influx into the IM or into the cytosol. Finally, J_{in} was replaced by $h_{icrac}J_{in}$, so that an increase in $[\text{Ca}^{2+}]$ at the IM causes inhibition of the CRAC channel, with time constant τ_{icrac} . Calcium moves from the IM to the cytosol at a rate proportional to the concentration difference of the two compartments, with rate constant 0.001/min. Other parameter values ($K_{icrac} = 0.05$ mM, $\tau_{icrac} = 5$ min) were chosen to give qualitative agreement with Figure 2A of (34) (as shown in Fig. S9).

Knockout simulations

The KO simulations of Figure 11 could not be performed on models 1, 3, and 6 for technical reasons.

Model 1 models mitochondria as a simple Ca²⁺ buffer with the usual buffering kinetics and with a fixed total amount of buffer (*i.e.*, with no proper MCU or NCLX modeling). Since model 1 contains no specific models of either the MCU or the NCLX, simulations of MCU or NCLX KO would be arbitrary and unreliable at best. Model 3 is a closed-cell model (*i.e.*, with no Ca²⁺ transport across the PM), which again is incompatible with KO experiments that change the total Ca²⁺ in the cell, making KO simulations impossible. Finally, model 6 is unable to simulate MCU/NCLX KO owing to resultant instabilities in the model. We do not yet understand the source of these instabilities, which remain a topic of current investigation.

Statistical analysis

All statistical analyses were performed using GraphPad Prism version 9. Statistically significant differences between groups were identified within the figures where *, **, ***, and **** indicate p -values of <0.05, <0.01, <0.001, and <0.0001,

respectively. Statistical significance or lack thereof are reported within the figure legends, and the type of statistical tests performed and resulting p -values from that test are recorded in supporting information.

Data availability

Statistical analyses and raw data of all experiments herein, including images of unprocessed Westerns, are included in a separate file. All original cell lines reported herein are available from the lead investigator upon request and completion of an MTA.

Supporting information—This article contains supporting information.

Acknowledgments—We are grateful to Dr Priya Santhanam (Penn State University) for help and advice on Ca²⁺ measurements in permeabilized cells and for giving us unlimited access to her PTI imaging system, Dr Suresh Joseph (Thomas Jefferson University) for the kind gift of HeLa cells and their MCU-KO clone, Dr John W. Elrod (Temple University) for kindly providing us with the MCU^{flx/flx} mice, and Drs Jeff Lock and Ian Parker (University of California, Irvine) for their advice and help with the Ca²⁺ puff measurements using TIRF microscopy and with data analysis.

Author contributions—R. E. Y., S. M. E., D. I. Y., J. S., M. T., J. M. H., and G. D. conceptualization; R. E. Y., S. M. E., P. X., D. I. Y., J. S., and M. T. methodology; R. E. Y., S. M. E., D. I. Y., J. S., and M. T. validation; R. E. Y., S. M. E., M. T., M. H., G. D., J. S., X. Z., V. A., and D. I. Y. formal analysis; R. E. Y., S. M. E., X. Z., P. X., V. A., T. P., J. C. B., M. T. J., A. E. A., and N. L. investigation; N. H., J. M. H., G. D., D. I. Y., J. S., M. T., and N. H. resources; R. E. Y., S. M. E., D. I. Y., J. S., and M. T. data curation; R. E. Y. and M. T. writing—original draft; N. H. and M. T. writing—review & editing; R. E. Y., S. M. E. and M. T. visualization; N. H., D. I. Y., and M. T. supervision; M. T. project administration; M. T. funding acquisition.

Funding and additional information—This work was supported by NHLBI, National Institutes of Health (R35-HL150778 to M. T.); NHLBI, National Institutes of Health (R01 HL137852 to Scott Earley and M. T.); NIDCR, National Institutes of Health (R01 DE019245 to D. I. Y. and J. S.); NCI, National Institutes of Health (R01 CA242021 to N. H.); and the NIDDK, National Institutes of Health Intramural Research Program (to J. M. H.). The content is solely the responsibility of the authors and does not necessarily represent the official views of the National Institutes of Health.

Conflict of interest—The authors declare that they have no conflicts of interest with the contents of this article.

Abbreviations—The abbreviations used are: 4-OHT, 4-hydroxytamoxifen; BCR, B cell receptor; CDI, Ca²⁺-dependent inactivation; CRAC, Ca²⁺ release-activated Ca²⁺; CCh, Carbachol; ER, endoplasmic reticulum; FCCP, trifluoromethoxy carbonylcyanide phenylhydrazone; IM, I_{CRAC} microdomain; IP₃, inositol-1,4,5-trisphosphate; IP₃R, IP₃ receptor; LPS, lipopolysaccharide; MAM, mitochondria-associated membrane; MCU, mitochondrial Ca²⁺ uniporter; NCLX, mitochondrial Na⁺/Ca²⁺ exchanger; NFAT, nuclear factor for activated T cells; PM, plasma membrane; RBL, rat basophilic leukemia; SERCA, sarcoplasmic/ER Ca²⁺ ATPase; SOCE,

store-operated Ca²⁺ entry; STIM, stromal interaction molecule; Tg, thapsigargin; TIRE, total internal reflection fluorescence.

References

- Tait, S. W., and Green, D. R. (2012) Mitochondria and cell signalling. *J. Cell Sci.* **125**, 807–815
- Chandel, N. S. (2015) Evolution of mitochondria as signaling organelles. *Cell Metab.* **22**, 204–206
- Bagur, R., and Hajnoczky, G. (2017) Intracellular Ca(2+) sensing: Its role in calcium homeostasis and signaling. *Mol. Cell* **66**, 780–788
- De Stefani, D., Rizzuto, R., and Pozzan, T. (2016) Enjoy the trip: Calcium in mitochondria back and forth. *Annu. Rev. Biochem.* **85**, 161–192
- Finkel, T., Menazza, S., Holmström, K. M., Parks, R. J., Liu, J., Sun, J., Liu, J., Pan, X., and Murphy, E. (2015) The ins and outs of mitochondrial calcium. *Circ. Res.* **116**, 1810–1819
- Hempel, N., and Trebak, M. (2017) Crosstalk between calcium and reactive oxygen species signaling in cancer. *Cell Calcium* **63**, 70–96
- Kamer, K. J., and Mootha, V. K. (2015) The molecular era of the mitochondrial calcium uniporter. *Nat. Rev. Mol. Cell Biol.* **16**, 545–553
- Pathak, T., and Trebak, M. (2018) Mitochondrial Ca(2+) signaling. *Pharmacol. Ther.* **192**, 112–123
- Baughman, J. M., Perocchi, F., Girgis, H. S., Plovnich, M., Belcher-Timme, C. A., Sancak, Y., Bao, X. R., Strittmatter, L., Goldberger, O., Bogorad, R. L., Kotliansky, V., and Mootha, V. K. (2011) Integrative genomics identifies MCU as an essential component of the mitochondrial calcium uniporter. *Nature* **476**, 341–345
- De Stefani, D., Raffaello, A., Teardo, E., Szabó, I., and Rizzuto, R. (2011) A forty-kilodalton protein of the inner membrane is the mitochondrial calcium uniporter. *Nature* **476**, 336–340
- Csordas, G., Golenar, T., Seifert, E. L., Kamer, K. J., Sancak, Y., Perocchi, F., Moffat, C., Weaver, D., Perez, S. F., Bogorad, R., Kotliansky, V., Adjianto, J., Mootha, V. K., and Hajnoczky, G. (2013) MICU1 controls both the threshold and cooperative activation of the mitochondrial Ca(2+)(+) uniporter. *Cell Metab.* **17**, 976–987
- Mallilankaraman, K., Doonan, P., Cardenas, C., Chandramoorthy, H. C., Muller, M., Miller, R., Hoffman, N. E., Gandhirajan, R. K., Molgo, J., Birnbaum, M. J., Rothberg, B. S., Mak, D. O., Foskett, J. K., and Madesh, M. (2012) MICU1 is an essential gatekeeper for MCU-mediated mitochondrial Ca(2+) uptake that regulates cell survival. *Cell* **151**, 630–644
- Payne, R., Hoff, H., Roskowski, A., and Foskett, J. K. (2017) MICU2 restricts spatial crosstalk between InsP3R and MCU channels by regulating threshold and gain of MICU1-mediated inhibition and activation of MCU. *Cell Rep.* **21**, 3141–3154
- Kamer, K. J., Grabarek, Z., and Mootha, V. K. (2017) High-affinity cooperative Ca(2+) binding by MICU1-MICU2 serves as an on-off switch for the uniporter. *EMBO Rep.* **18**, 1397–1411
- Perocchi, F., Gohil, V. M., Girgis, H. S., Bao, X. R., McCombs, J. E., Palmer, A. E., and Mootha, V. K. (2010) MICU1 encodes a mitochondrial EF hand protein required for Ca(2+) uptake. *Nature* **467**, 291–296
- Kamer, K. J., Jiang, W., Kaushik, V. K., Mootha, V. K., and Grabarek, Z. (2019) Crystal structure of MICU2 and comparison with MICU1 reveal insights into the uniporter gating mechanism. *Proc. Natl. Acad. Sci. U. S. A.* **116**, 3546
- Palty, R., Hershinkel, M., and Sekler, I. (2012) Molecular identity and functional properties of the mitochondrial Na⁺/Ca²⁺ exchanger. *J. Biol. Chem.* **287**, 31650–31657
- Jiang, D., Zhao, L., and Clapham, D. E. (2009) Genome-wide RNAi screen identifies Letm1 as a mitochondrial Ca²⁺/H⁺ antiporter. *Science* **326**, 144–147
- Csordas, G., Renken, C., Varnai, P., Walter, L., Weaver, D., Buttle, K. F., Balla, T., Mannella, C. A., and Hajnoczky, G. (2006) Structural and functional features and significance of the physical linkage between ER and mitochondria. *J. Cell Biol.* **174**, 915–921
- Berridge, M. J. (2016) The inositol trisphosphate/calcium signaling pathway in health and disease. *Physiol. Rev.* **96**, 1261–1296
- Prakriya, M., and Lewis, R. S. (2015) Store-operated calcium channels. *Physiol. Rev.* **95**, 1383–1436
- Trebak, M., and Kinet, J. P. (2019) Calcium signalling in T cells. *Nat. Rev. Immunol.* **19**, 154–169
- Trebak, M., and Putney, J. W., Jr. (2017) ORAI calcium channels. *Physiology (Bethesda)* **32**, 332–342
- Dupont, G., Combettes, L., Bird, G. S., and Putney, J. W. (2011) Calcium oscillations. *Cold Spring Harb. Perspect. Biol.* **3**, a004226
- Sneyd, J., Han, J. M., Wang, L., Chen, J., Yang, X., Tanimura, A., Sanderson, M. J., Kirk, V., and Yule, D. I. (2017) On the dynamical structure of calcium oscillations. *Proc. Natl. Acad. Sci. U. S. A.* **114**, 1456
- Dolmetsch, R. E., and Lewis, R. S. (1994) Signaling between intracellular Ca²⁺ stores and depletion-activated Ca²⁺ channels generates [Ca²⁺]_i oscillations in T lymphocytes. *J. Gen. Physiol.* **103**, 365–388
- Gwack, Y., Feske, S., Srikanth, S., Hogan, P. G., and Rao, A. (2007) Signalling to transcription: Store-operated Ca²⁺ entry and NFAT activation in lymphocytes. *Cell Calcium* **42**, 145–156
- Vaeth, M., and Feske, S. (2018) NFAT control of immune function: New frontiers for an abiding trooper. *FI000Res* **7**, 260
- Vaeth, M., Maus, M., Klein-Hessling, S., Freinkman, E., Yang, J., Eckstein, M., Cameron, S., Turvey, S. E., Serfling, E., Berberich-Siebelt, F., Possemato, R., and Feske, S. (2017) Store-operated Ca(2+) entry controls clonal expansion of T cells through metabolic reprogramming. *Immunity* **47**, 664–679.e666
- Mullins, F. M., and Lewis, R. S. (2016) The inactivation domain of STIM1 is functionally coupled with the Orai1 pore to enable Ca²⁺-dependent inactivation. *J. Gen. Physiol.* **147**, 153–164
- Mullins, F. M., Yen, M., and Lewis, R. S. (2016) Orai1 pore residues control CRAC channel inactivation independently of calmodulin. *J. Gen. Physiol.* **147**, 137–152
- Zhang, X., Pathak, T., Yoast, R., Emrich, S., Xin, P., Nwokonko, R. M., Johnson, M., Wu, S., Delierieux, C., Gueguinou, M., Hempel, N., Putney, J. W., Gill, D. L., and Trebak, M. (2019) A calcium/cAMP signaling loop at the ORAI1 mouth drives channel inactivation to shape NFAT induction. *Nat. Commun.* **10**, 1971
- Zweifach, A., and Lewis, R. S. (1995) Rapid inactivation of depletion-activated calcium current (ICRAC) due to local calcium feedback. *J. Gen. Physiol.* **105**, 209–226
- Zweifach, A., and Lewis, R. S. (1995) Slow calcium-dependent inactivation of depletion-activated calcium current. Store-dependent and -independent mechanisms. *J. Biol. Chem.* **270**, 14445–14451
- Li, X., Wu, G., Yang, Y., Fu, S., Liu, X., Kang, H., Yang, X., Su, X. C., and Shen, Y. (2017) Calmodulin dissociates the STIM1-Orai1 complex and STIM1 oligomers. *Nat. Commun.* **8**, 1042
- Hoth, M., Button, D. C., and Lewis, R. S. (2000) Mitochondrial control of calcium-channel gating: A mechanism for sustained signaling and transcriptional activation in T lymphocytes. *Proc. Natl. Acad. Sci. U. S. A.* **97**, 10607–10612
- Hoth, M., Fanger, C. M., and Lewis, R. S. (1997) Mitochondrial regulation of store-operated calcium signaling in T lymphocytes. *J. Cell Biol.* **137**, 633–648
- Samanta, K., Douglas, S., and Parekh, A. B. (2014) Mitochondrial calcium uniporter MCU supports cytoplasmic Ca²⁺ oscillations, store-operated Ca²⁺ entry and Ca²⁺-dependent gene expression in response to receptor stimulation. *PLoS One* **9**, e101188
- Quintana, A., Pasche, M., Junker, C., Al-Ansary, D., Rieger, H., Kummerow, C., Nunez, L., Villalobos, C., Meraner, P., Becherer, U., Rettig, J., Niemeyer, B. A., and Hoth, M. (2011) Calcium microdomains at the immunological synapse: How ORAI channels, mitochondria and calcium pumps generate local calcium signals for efficient T-cell activation. *EMBO J.* **30**, 3895–3912
- Berry, C. T., Liu, X., Myles, A., Nandi, S., Chen, Y. H., Hershberg, U., Brodsky, I. E., Cancro, M. P., Lengner, C. J., May, M. J., and Freedman, B. D. (2020) BCR-induced Ca(2+) signals dynamically tune survival, metabolic reprogramming, and proliferation of naive B cells. *Cell Rep.* **31**, 107474

41. Matsumoto, M., Fujii, Y., Baba, A., Hikida, M., Kurosaki, T., and Baba, Y. (2011) The calcium sensors STIM1 and STIM2 control B cell regulatory function through interleukin-10 production. *Immunity* **34**, 703–714
42. Emrich, S. M., Yoast, R. E., Xin, P., Arige, V., Wagner, L. E., Hempel, N., Gill, D. L., Sneyd, J., Yule, D. I., and Trebak, M. (2021) Omnitemporal choreographies of all five STIM/Orai and IP3Rs underlie the complexity of mammalian Ca(2+) signaling. *Cell Rep.* **34**, 108760
43. Yoast, R. E., Emrich, S. M., Zhang, X., Xin, P., Johnson, M. T., Fike, A. J., Walter, V., Hempel, N., Yule, D. I., Sneyd, J., Gill, D. L., and Trebak, M. (2020) The native ORAI channel trio underlies the diversity of Ca(2+) signaling events. *Nat. Commun.* **11**, 2444
44. Wacquier, B., Combettes, L., Van Nhieu, G. T., and Dupont, G. (2016) Interplay between intracellular Ca(2+) oscillations and Ca(2+)-stimulated mitochondrial metabolism. *Sci. Rep.* **6**, 19316
45. Fall, C. P., and Keizer, J. E. (2001) Mitochondrial modulation of intracellular Ca(2+) signaling. *J. Theor. Biol.* **210**, 151–165
46. Magnus, G. G., and Keizer, J. J. (1997) Minimal model of beta-cell mitochondrial Ca²⁺ handling. *Am. J. Physiol.* **273**, C717–C733
47. Han, J. M., and Periwál, V. (2019) A mathematical model of calcium dynamics: Obesity and mitochondria-associated ER membranes. *PLoS Comput. Biol.* **15**, e1006661
48. Ben-Kasus Nissim, T., Zhang, X., Elazar, A., Roy, S., Stolwijk, J. A., Zhou, Y., Motiani, R. K., Gueguinou, M., Hempel, N., Hershinkel, M., Gill, D. L., Trebak, M., and Sekler, I. (2017) Mitochondria control store-operated Ca(2+) entry through Na(+) and redox signals. *EMBO J.* **36**, 797–815
49. Pozzan, T., Magalhaes, P., and Rizzuto, R. (2000) The comeback of mitochondria to calcium signalling. *Cell Calcium* **28**, 279–283
50. Denton, R. M., and McCormack, J. G. (1990) Ca²⁺ as a second messenger within mitochondria of the heart and other tissues. *Annu. Rev. Physiol.* **52**, 451–466
51. Hajnóczky, G., Robb-Gaspers, L. D., Seitz, M. B., and Thomas, A. P. (1995) Decoding of cytosolic calcium oscillations in the mitochondria. *Cell* **82**, 415–424
52. Rizzuto, R., Marchi, S., Bonora, M., Aguiari, P., Bononi, A., De Stefani, D., Giorgi, C., Leo, S., Rimessi, A., Siviero, R., Zecchini, E., and Pinton, P. (2009) Ca(2+) transfer from the ER to mitochondria: When, how and why. *Biochim. Biophys. Acta* **1787**, 1342–1351
53. Samanta, K., Bakowski, D., Amin, N., and Parekh, A. B. (2020) The whole-cell Ca²⁺ release-activated Ca²⁺ current, ICRAC, is regulated by the mitochondrial Ca²⁺ uniporter channel and is independent of extracellular and cytosolic Na⁺. *J. Physiol.* **598**, 1753–1773
54. Korzeniowski, M. K., Szanda, G., Balla, T., and Spat, A. (2009) Store-operated Ca²⁺ influx and subplasmalemmal mitochondria. *Cell Calcium* **46**, 49–55
55. Naghdi, S., Waldeck-Weiermair, M., Fertschaj, I., Poteser, M., Graier, W. F., and Malli, R. (2010) Mitochondrial Ca²⁺ uptake and not mitochondrial motility is required for STIM1-Orai1-dependent store-operated Ca²⁺ entry. *J. Cell Sci.* **123**, 2553–2564
56. Quintana, A., and Hoth, M. (2012) Mitochondrial dynamics and their impact on T cell function. *Cell Calcium* **52**, 57–63
57. Forkink, M., Basit, F., Teixeira, J., Swarts, H. G., Koopman, W. J. H., and Willems, P. (2015) Complex I and complex III inhibition specifically increase cytosolic hydrogen peroxide levels without inducing oxidative stress in HEK293 cells. *Redox Biol.* **6**, 607–616
58. Brand, M. D. (2016) Mitochondrial generation of superoxide and hydrogen peroxide as the source of mitochondrial redox signaling. *Free Radic. Biol. Med.* **100**, 14–31
59. Bogeski, I., Kummerow, C., Al-Ansary, D., Schwarz, E. C., Koehler, R., Kozai, D., Takahashi, N., Peinelt, C., Griesemer, D., Bozem, M., Mori, Y., Hoth, M., and Niemeyer, B. A. (2010) Differential redox regulation of ORAI ion channels: A mechanism to tune cellular calcium signaling. *Sci. Signal* **3**, ra24
60. Quintana, A., Schwarz, E. C., Schwindling, C., Lipp, P., Kaestner, L., and Hoth, M. (2006) Sustained activity of calcium release-activated calcium channels requires translocation of mitochondria to the plasma membrane. *J. Biol. Chem.* **281**, 40302–40309
61. Quintana, A., Schwindling, C., Wenning, A. S., Becherer, U., Rettig, J., Schwarz, E. C., and Hoth, M. (2007) T cell activation requires mitochondrial translocation to the immunological synapse. *Proc. Natl. Acad. Sci. U. S. A.* **104**, 14418–14423
62. Crabtree, G. R., and Olson, E. N. (2002) NFAT signaling: Choreographing the social lives of cells. *Cell* **109 Suppl**, S67–S79
63. Koval, O. M., Nguyen, E. K., Santhana, V., Fidler, T. P., Sebag, S. C., Rasmussen, T. P., Mittauer, D. J., Strack, S., Goswami, P. C., Abel, E. D., and Grumbach, I. M. (2019) Loss of MCU prevents mitochondrial fusion in G1-S phase and blocks cell cycle progression and proliferation. *Sci. Signal* **12**
64. Zhao, H., Li, T., Wang, K., Zhao, F., Chen, J., Xu, G., Zhao, J., Li, T., Chen, L., Li, L., Xia, Q., Zhou, T., Li, H. Y., Li, A. L., Finkel, T., et al. (2019) AMPK-mediated activation of MCU stimulates mitochondrial Ca(2+) entry to promote mitotic progression. *Nat. Cell Biol.* **21**, 476–486
65. Wacquier, B., Combettes, L., and Dupont, G. (2019) Cytoplasmic and mitochondrial calcium signaling: A two-way relationship. *Cold Spring Harbor Perspect. Biol.* **11**, a035139
66. Ishii, K., Hirose, K., and Iino, M. (2006) Ca²⁺ shuttling between endoplasmic reticulum and mitochondria underlying Ca²⁺ oscillations. *EMBO Rep.* **7**, 390–396
67. Lock, J. T., Ellefsen, K. L., Settle, B., Parker, I., and Smith, I. F. (2015) Imaging local Ca²⁺ signals in cultured mammalian cells. *J. Vis. Exp.*, 52516
68. Ellefsen, K. L., Settle, B., Parker, I., and Smith, I. F. (2014) An algorithm for automated detection, localization and measurement of local calcium signals from camera-based imaging. *Cell Calcium* **56**, 147–156
69. Lock, J. T., Alzayady, K. J., Yule, D. I., and Parker, I. (2018) All three IP3 receptor isoforms generate Ca(2+) puffs that display similar characteristics. *Sci. Signal* **11**, eaau0344
70. Mataragka, S., and Taylor, C. W. (2018) All three IP3 receptor subtypes generate Ca(2+) puffs, the universal building blocks of IP3-evoked Ca(2+) signals. *J. Cell Sci.* **131**, jcs220848
71. Gonzalez-Cobos, J. C., Zhang, X., Zhang, W., Ruhle, B., Motiani, R. K., Schindl, R., Muik, M., Spinelli, A. M., Bisailon, J. M., Shinde, A. V., Fahrner, M., Singer, H. A., Matrougui, K., Barroso, M., Romanin, C., et al. (2013) Store-independent Orai1/3 channels activated by intracrine leukotriene C₄: role in neointimal hyperplasia. *Circ. Res.* **112**, 1013–1025
72. Zhang, X., González-Cobos, J. C., Schindl, R., Muik, M., Ruhle, B., Motiani, R. K., Bisailon, J. M., Zhang, W., Fahrner, M., Barroso, M., Matrougui, K., Romanin, C., and Trebak, M. (2013) Mechanisms of STIM1 activation of store-independent leukotriene C₄-regulated Ca²⁺ channels. *Mol. Cell. Biol.* **33**, 3715–3723
73. Zhang, X., Zhang, W., González-Cobos, J. C., Jardin, I., Romanin, C., Matrougui, K., and Trebak, M. (2014) Complex role of STIM1 in the activation of store-independent Orai1/3 channels. *J. Gen. Physiol.* **143**, 345–359
74. Luongo, T. S., Lambert, J. P., Yuan, A., Zhang, X., Gross, P., Song, J., Shanmughapriya, S., Gao, E., Jain, M., Houser, S. R., Koch, W. J., Cheung, J. Y., Madesh, M., and Elrod, J. W. (2015) The mitochondrial calcium uniporter matches energetic supply with cardiac workload during stress and modulates permeability transition. *Cell Rep.* **12**, 23–34
75. Aghajani, K., Keerthivasan, S., Yu, Y., and Gounari, F. (2012) Generation of CD4CreER(T²) transgenic mice to study development of peripheral CD4-T-cells. *Genesis* **50**, 908–913
76. Hobeika, E., Thiemann, S., Storch, B., Jumaa, H., Nielsen, P. J., Pelanda, R., and Reth, M. (2006) Testing gene function early in the B cell lineage in mb1-cre mice. *Proc. Natl. Acad. Sci. U. S. A.* **103**, 13789–13794

EDITORS' PICK: *MCU regulation of interorganellar Ca²⁺ transfer and NFAT*



Ryan E. Yoast recently completed his PhD in biomedical sciences at the Pennsylvania State University College of Medicine. During his doctoral training, he determined how the coordinated functions of multiple Ca²⁺ channels and sensors shape the native cytosolic Ca²⁺ signal of numerous cell types. He is now leveraging his molecular biology and genome editing training to identify novel druggable targets in inflammatory and autoimmune diseases.